Reconstruction of an Inductive Velocity Field Vector from Doppler Motions and a Pair of Solar Vector Magnetograms

Manolis K. Georgoulis & Barry J. LaBonte

The Johns Hopkins University Applied Physics Laboratory, 11100 Johns Hopkins Rd., Laurel, MD 20723, USA

ABSTRACT

We outline a general methodology to infer the inductive velocity field vector in solar active regions. For the first time, both the field-aligned and the cross-field velocity components are reconstructed. The cross-field velocity solution accounts for the changes of the vertical magnetic field seen between a pair of successive active-region vector magnetograms via the ideal induction equation. The field-aligned velocity is obtained using the Doppler velocity and the calculated cross-field velocity. Solving the ideal induction equation in vector magnetograms measured at a given altitude in the solar atmosphere is an under-determined problem. In response, our general formalism allows the use of any additional constraint for the inductive cross-field velocity to enforce a unique solution in the induction equation. As a result, our methodology can give rise to new velocity solutions besides the one presented here. To constrain the induction equation, we use a special case of the minimum structure approximation that was introduced in previous studies and is already employed here to resolve the 180°-ambiguity in the input vector magnetograms. We reconstruct the inductive velocity for three active regions, including NOAA AR 8210 for which previous results exist. Our solution believably reproduces the horizontal flow patterns in the studied active regions but breaks down in cases of localized rapid magnetic flux emergence or submergence. Alternative approximations and constraints are possible and can be accommodated into our general formalism.

Subject headings: MHD—Sun: atmospheric motions—Sun: magnetic fields—Sun: photosphere

1. Introduction

Despite recent advances in vector magnetography, reliable measurement of the magnetic field vector in the solar active-region atmosphere can be routinely performed only at

photospheric heights. In view of the central role of the magnetic field in the dynamical evolution and the eruptive manifestations in the solar atmosphere, the photospheric magnetic field vector should then be fully exploited to allow an assessment of the three-dimensional (3D) magnetic structures above the photosphere. Magnetic field extrapolations provide a means to calculate the chromospheric and coronal magnetic fields using the photospheric fields as the required boundary condition. Extrapolation techniques use approaches of various sophistication levels, such as the current-free approximation (Schmidt 1964), the linear force-free (Alissandrakis 1981), or the nonlinear force-free approximation (Amari, Boulmezaoud, & Mikić 1999). Nonetheless, non-force-free extrapolations are probably the most realistic approach, given that the photospheric magnetic fields are forced (Metcalf et al. 1995; Georgoulis & LaBonte 2004). The non-force-free modeling of the coronal magnetic fields requires the equations of Magnetohydrodynamics (MHD). Development of 3D MHD models has become possible due to the steadily increasing computing capabilities. These models are promising for understanding the pre-event configuration of solar eruptions and coronal mass ejections (CMEs), as well as the role of current sheets, turbulence, and kinematic effects in the solar atmosphere (see, e.g., Gudiksen & Nordlund 2002; Amari et al. 2003). A particularly appealing aspect of 3D MHD models is that they can be data-driven, i.e., they can utilize boundary conditions corresponding to observed active region magnetic fields (Abbett 2003; Roussev et al. 2004). However, the electric fields, the magnetic forces, and the time-dependent parts of the MHD equations depend sensitively on the flows of the magnetized plasma. Therefore, photospheric boundary information should include a reliable assessment of the velocity field vector in addition to the magnetic field vector.

The coupling between the photospheric magnetic and velocity fields also pertains to the calculation of the magnetic helicity in solar active regions (see Berger 1999 for an introduction). Helicity studies are important because they may imply a potential forecasting capability for solar flares and CMEs. Berger & Field (1984) derived the Poynting theorem of magnetic helicity in an open volume. This expression enables the calculation of the temporal variation of the relative magnetic helicity above the boundary plane of the magnetic field measurements but employs explicitly the velocity field vector on the boundary plane.

Measurements of the photospheric magnetic field vector are routine but the photospheric velocity is only partially measured. Its longitudinal component can be inferred from the Doppler effect on the spectral line used for the magnetic field observations. However, the measurement of the Doppler velocity is subject to a number of caveats and ambiguities (see, e.g., Chae, Moon, & Pevtsov 2004 for a discussion). In addition, the Doppler signal is affected by oscillatory effects, such as the $5 - min$ oscillations, while its amplitude depends on the employed inference technique, with more than one such techniques existing. As a result, the Doppler velocity requires very careful handling. In addition, the Doppler velocity does not

provide any information about the transverse (i.e. perpendicular to the line-of-sight) flows. Even if the problems associated with the Doppler velocity were resolved and even if the transverse velocity could be measured on the magnetically sensitive spectral line, however, knowledge of the photospheric flow field in solar active regions would still be partial. This is because the photospheric plasma is a mixture of magnetized and unmagnetized elements. Non-magnetized plasma flows have minimal impact on the magnetic field measurements and hence they cannot be inferred from the magnetically sensitive spectral line. This fact, however, may has a positive side since the knowledge of the purely hydrodynamic (HD) flows may not be crucial for the study of magnetic fields and their evolution.

The first method used to infer the unknown transverse photospheric flows was the *local correlation tracking* (LCT) technique of November & Simon (1988). The LCT algorithm measures the displacements of the various patterns present in a pair of white-light continuum images and finds an average velocity associated with these displacements under the assumption that the motions causing the displacements are smooth. A major requirement for the LCT method to work is that the studied patterns must exhibit significant contrast differences to be followed effectively in time. Moreover, the patterns must maintain their structural integrity for time scales much larger than the cadence of the observations since a continuous restructuring would make tracking problematic. The above two requirements are fulfilled in the quiet photospheric filigree observed in optical wavelengths, so the LCT technique is undoubtedly the best way to infer the transverse HD flows of the mostly unmagnetized quiet solar photosphere. November & Simon (1988) showed that the LCT velocity successfully reproduces the quiet-Sun granular convective motion. Tracking algorithms have been implemented in a number of schemes, such as the "feature tracking" method of Strous et al. (1996), the LCT technique of Berger et al. (1998), and the "balltracking" technique of Potts, Barrett, & Diver (2004).

Despite its importance in quiet-Sun velocity measurements, the LCT technique is problematic in the active-region photosphere. First, it is not clear which input would give more appropriate results to LCT algorithms, as both the continuum images and the magnetogram images reveal different aspects of the photospheric flows. Applying the two different inputs leads to two different results. Second, both the white-light and the magnetogram structures in active regions may reform too rapidly for flows to be inferred with sufficient detail. The photospheric filigree is present but disrupted because of the widespread strong magnetic flux, while rapid restructuring of the emerging magnetic structures, especially in emerging flux regions, introduces uncertainties in the LCT results. Consequently, it is not uncommon for the LCT velocity to require significant averaging in order to yield results consistent with a visual inspection of the observed flows in active regions. Even averaging needs to be performed carefully to avoid propagation of systematic errors (Roudier et al. 1999). Third, the LCT

technique requires a FWHM apodizing window whose size is typically a few times larger than the instrument's pixel size. Therefore, the LCT flow maps are coarser than the employed input maps. This is because the LCT maximizes the cross-correlation function by applying displacements to the initial tiled image and by comparing the result with the second image of the pair, so each apodization tile must contain sufficient structure to yield a well-defined peak of the cross-correlation function. Different choices of the apodizing window reflect different types of flows and give different results, since the kinetic power is distributed over a variety of spatial scales in an active region. Small tile sizes tend to reveal the small-scale convection while large tile sizes reproduce the systematic flows seen during the emergence of the magnetic dipole(s) that eventually form an active region. Fourth, some systematic motions do not even correspond to actual flows, but they are apparent and caused by the projected emergence of inclined magnetic structures. Tracking techniques tend to attribute a systematic transverse velocity to these purely vertical flows. In summary, as an active region traverses far from disk center, the LCT velocity provides a crude, as well as inextricable, mixture of HD flows, MHD flows, horizontal and vertical flows, and apparent flows caused by projection effects.

Given that the velocity field acting on a given magnetic field is required to calculate the magnetic helicity flux on the plane of the observations, several authors (e.g., Moon et al. 2002; Nindos & Zhang 2002; Romano, Contarino, & Zuccarello 2003) have used the LCT velocity inferred by photospheric magnetograms after Chae (2001) developed a technique to evaluate the Poynting theorem of Berger & Field (1984). In these studies, the LCT velocity is assumed representative of the actual horizontal velocity which is inaccurate even at moderate distances from disk center. Moreover, the impact of the apparent transverse flows caused by projection effects is not removed. Démoulin & Berger (2003) quantified this effect by showing that the LCT velocity $\mathbf{v_{LCT}}$ relates to both the actual vertical velocity u_z and the actual horizontal velocity $\mathbf{u_h}$ via a relation of the form

$$\mathbf{u_h} = \frac{u_z}{B_z}\mathbf{B_h} + \mathbf{v_{LCT}} \quad , \tag{1}$$

where B_z and $\mathbf{B_h}$ are the vertical magnetic field and the horizontal magnetic field vector, respectively (considering the spherical geometry of the Sun, these components can be equivalently called the normal and the tangential to the photosphere components, respectively). From equation (1) we notice that the LCT velocity can be very different from the actual horizontal velocity $\mathbf{u_h}$ in the presence of large magnetic fluxes and emerging or submerging inclined magnetic configurations.

Since MHD simulations and magnetic helicity calculations require a velocity field vector that reflects the evolution of the magnetic field and the magnetized plasma flows, an alternative way to calculate the velocity is to demand minimum compliance with the MHD

equations. A fundamental time-dependent MHD equation is the induction equation

$$\frac{\partial \mathbf{B}}{\partial t} = \nabla \times (\mathbf{u} \times \mathbf{B}) + \eta \nabla^2 \mathbf{B} \ , \tag{2}$$

where the action of the velocity field $\mathbf{u}$ on the magnetic field $\mathbf{B}$ together with the diffusion of the magnetic field subject to a magnetic diffusivity η are responsible for the temporal variation of the magnetic field. To solve equation (2) for $\mathbf{u}$ it is necessary to adhere to the ideal limit of the induction equation, i.e. to assume that the diffusive term $\eta \nabla^2 \mathbf{B}$ is negligible. Furthermore, single-height (i.e. photospheric) vector magnetic field measurements preclude direct knowledge of the vertical gradient $(\partial / \partial z)$ of any measured quantity. As a result, we can only tackle the vertical component of the ideal MHD induction equation, namely,

$$\frac{\partial B_z}{\partial t} = [\nabla \times (\mathbf{u} \times \mathbf{B})]_z \ . \tag{3}$$

The goal, then, is to solve equation (3) for $\mathbf{u}$ using a pair of vector magnetograms to calculate $(\partial B_z / \partial t)$. A major drawback to this objective is that the problem is under-determined: the induction equation (3) by itself does not have a unique solution. Evidently, only the cross-field (i.e. perpendicular to the magnetic field vector) velocity $\mathbf{u}_\perp$ participates in the induction equation. This contributes a condition additional to the ideal induction equation (3), namely the orthogonality of the $\mathbf{u}_\perp$-solution with $\mathbf{B}$, $\mathbf{u}_\perp \cdot \mathbf{B} = 0$. As a result, only two equations are available to infer the three components of $\mathbf{u}_\perp$. An additional assumption or constraint may lead to a third equation and hence to a unique solution of equation (3). Since only $\mathbf{u}_\perp$ participates in the induction equation, the field-aligned velocity $\mathbf{u}_{||}$ can only be inferred by additional assumptions, independent of the induction equation.

Kusano et al. (2002) first devised a technique to constrain the induction equation (3) by utilizing the LCT velocity. The latter was assumed representative of the actual horizontal velocity and then the induction equation (3) was solved for the vertical velocity. Next, Welsch et al. (2004) explicitly employed the geometrical expression of Démoulin & Berger (equation (1) and $\mathbf{v_{LCT}}$. By means of the orthogonality condition, $\mathbf{u}_\perp \cdot \mathbf{B} = 0$, equation (1) and equation (3), then, they were able to obtain a unique [called the inductive LCT (ILCT)] solution for $\mathbf{u}_\perp$.

The "hybrid" techniques of Kusano et al. (2002) and Welsch et al. (2004) are certainly advancements over a simple use of the LCT velocity but but they give rise to a number of issues:

(1) The LCT velocity may be inconsistent with the induction equation, since (i) MHD is not used to infer the LCT velocity, (ii) the LCT velocity reflects a mixture of HD, MHD, and apparent flows, measured on a coarser scale than the corresponding vector

magnetograms, and (iii) the LCT results depend on the choice of the FWHM apodizing window.

(2) The use of the LCT velocity may enforce a unique solution of the induction equation, but the LCT velocity itself is *not* unique. A different LCT result gives rise to a different inductive velocity $\mathbf{u}_\perp$. How sensitively $\mathbf{u}_\perp$ depends $\mathbf{v_{LCT}}$ is unknown.

The first inductive technique for a $\mathbf{u}_\perp$ disentangled from the LCT velocity was developed by Longcope (2004) who found a parametric family of solutions of the induction equation (3) and then selected the solution with minimal flow speed. Longcope's (2004) minimum energy fit (MEF) technique is an excellent development. The MEF hypothesis is reasonable, appropriate for helicity studies, and most probably consistent with 3D MHD models. Nevertheless, it is not clear whether the complicated evolution of complex, dynamic active regions is consistent with an assumption of minimum flows.

Notice that all the above inductive techniques consider only the cross-field velocity $\mathbf{u}_\perp$ and make no attempt to calculate the field-aligned velocity $\mathbf{u}_{||}$.

In this study, we generalize the reconstruction of an inductive velocity field vector in solar active regions. We attempt a complete reconstruction including *both* the field-aligned and the cross-field velocity components that account for the change of the vertical magnetic field seen between a pair of observed vector magnetograms. First, we outline a general solving technique that allows *any* additional constraint for $\mathbf{u}_\perp$ to enforce a unique solution of the induction equation (3) for the cross-field velocity. Second, we calculate the field-aligned velocity by rotating the Doppler (longitudinal) velocity to the heliographic reference system. Like Longcope (2004) we refrain from using the LCT velocity. Our proposed constraint is a restricted *minimum structure* approximation. The unrestricted approximation was introduced by Georgoulis, LaBonte, & Metcalf (2004) to resolve the 180°-ambiguity in the orientation of the transverse magnetic field component in vector magnetogram measurements and is already employed here since we cannot apply the induction equation to a pair of 180°-ambiguous vector magnetograms. The restriction in the minimum structure approximation stems from assuming that the magnetic field $\mathbf{B}$, the cross-field velocity $\mathbf{u}_\perp$, and the cross-field gradient $(\nabla B)_\perp$ of the magnetic field strength are *coplanar*. This assumption implies that $\mathbf{u}_\perp$ directly relates to the gradients $(\nabla B)_\perp$ and aims to either sustain or relax them on the $[(\nabla B)_\perp, \mathbf{B}]$-plane. This "coplanar minimum structure approximation" enforces a unique solution of the induction equation (3) for $\mathbf{u}_\perp$. Together with the corresponding field-aligned velocity $\mathbf{u}_{||}$ we perform a complete *minimum structure reconstruction* (MSR) of the inductive velocity field. The general solution of the ideal induction equation (3) and the general calculation of the field-aligned velocity are discussed in §2. The analytical derivation of a velocity field consistent with the MHD equations is performed in §3. The special case of

the MSR velocity solution is derived and discussed in §4. The MSR velocity for three solar active regions is reconstructed in §5, while in §6 we discuss our physical assumptions and we summarize our findings.

2. General reconstruction of the inductive velocity field vector

2.1. Cross-field velocity: a general solution of the induction equation

A useful technique to treat the vertical component of the ideal induction equation has been described by Welsch et al. (2004) and Longcope (2004). The rhs of equation (3) can be transformed into the divergence of a vector as follows:

$$\frac{\partial B_z}{\partial t} = \nabla_h \cdot (v_z \mathbf{B_h} - B_z \mathbf{v_h}) \ , \tag{4}$$

where $\nabla_h = [(\partial/\partial x), (\partial/\partial y), 0]$. Then, by introducing two scalar potentials ϕ and ψ, termed a "stream function" and a "electrostatic potential", respectively, by Longcope (2004), the term in the parenthesis in equation (4) can be written as

$$v_z \mathbf{B_h} - B_z \mathbf{v_h} = \nabla_h \phi + \nabla_h \psi \times \hat{\mathbf{z}} \ . \tag{5}$$

To find a unique solution $\mathbf{u}_\perp$ for the inductive velocity $\mathbf{v}$, then, one has to specify uniquely the scalar potentials ϕ and ψ.

2.1.1. Calculating the stream function ϕ

There are at least two ways to find a unique solution for the stream function ϕ. The simplest way is to substitute equation (5) into equation (4). This yields a Poisson equation for ϕ on the horizontal plane, namely,

$$\frac{\partial B_z}{\partial t} = \nabla_h^2 \phi \ . \tag{6}$$

Equation (6) can be solved by means of a *successive over-relaxation* (SOR) technique or an *alternating-direction implicit* (ADI) technique (§2.3 and Press et al. 1992). The SOR algorithm is simpler, albeit computationally expensive for large grids. Equation (6) can be solved for ϕ on the horizontal plane S assuming homogeneous Dirichlet boundary conditions ($\phi = 0$) on ∂S. The calculation of ϕ alone yields a special inductive velocity $\mathbf{v}$ given by

$$\begin{aligned} \mathbf{v_h} &= (1/B_z)(-\nabla_h \phi + v_z \mathbf{B_h}) \\ v_z &= (1/B^2)\mathbf{B_h} \cdot \nabla_h \phi \ . \end{aligned} \tag{7}$$

To reach the special solution $\mathbf{v}$ we used the orthogonality condition $\mathbf{v} \cdot \mathbf{B} = 0$ in conjunction with equation (5) for $\psi = 0$.

Alternatively, one may write equation (3) as a flux-conservative equation on the horizontal plane, namely,

$$\nabla_{\mathbf{h}} \cdot \mathbf{F} = \frac{\partial B_z}{\partial t} \ , \tag{8}$$

where $\mathbf{F} = [(\mathbf{v} \times \mathbf{B})_y, -(\mathbf{v} \times \mathbf{B})_x, 0]$ is the conserved "flux" and $\mathbf{v}$ is the inductive velocity. If we assume that $\mathbf{v}$ is identical to the velocity of equations (7), obtained for $\psi = 0$, then the flux $\mathbf{F} = \nabla_h \phi$, and hence the stream function ϕ, can be calculated by means of a *timestep splitting* technique (Boris et al. 1993). The latter approach requires less computing time compared to the SOR and similar computing time to the ADI algorithm.

2.1.2. Calculating the electrostatic potential ψ

In previous inductive techniques the additional constraint used to enforce a unique solution of the ideal induction equation has been either the LCT velocity (Kusano et al. 2002; Welsch et al. 2004) or an assumption of minimal flows for the desired flow field (Longcope 2004). We hereby generalize the problem by uniquely specifying the electrostatic potential ψ when any one component of the desired solution $\mathbf{u}_\perp$ is assumed known on dependent on the other two components of $\mathbf{u}_\perp$. Without loss of generality we choose the vertical component $u_{\perp_z}$ of $\mathbf{u}_\perp$ as the prescribed component. Besides leading to a unique solution for $\mathbf{u}_\perp$, this action can reproduce the results of previous inductive techniques if these techniques' $u_{\perp_z}$-solution is introduced into our general solving methodology or it can give rise to new solutions if alternative prescriptions for $u_{\perp_z}$ are used.

To find a unique solution for ψ, recall the flux-conservative equation (8), where $\mathbf{F} = [(\mathbf{v} \times \mathbf{B})_y, -(\mathbf{v} \times \mathbf{B})_x, 0]$ is the flux and $\mathbf{v}$ is the special inductive velocity of equations (7). We realize that any flux $\mathbf{F}' = [(\mathbf{v}' \times \mathbf{B})_y, -(\mathbf{v}' \times \mathbf{B})_x, 0]$ is a solution of equation (8), and hence of the induction equation (3), if it satisfies the condition

$$\mathbf{F}' = \mathbf{F} + \mathbf{G} \ ; \quad with \quad \nabla_h \cdot \mathbf{G} = 0 \ . \tag{9}$$

Notice that $F_z = F'_z = 0$, so $G_z = 0$. Therefore, one may define two gauge conditions for $\mathbf{G}$ in the volume $z \geq 0$ and on the plane S ($z = 0$) of the magnetic field measurements, namely

$$\nabla \cdot \mathbf{G} = 0 \ , \quad and \quad \mathbf{G} \cdot \hat{\mathbf{z}}|_{z=0} = 0 \ . \tag{10}$$

Combining equations (5), (8), and (9) one finds that $\mathbf{G}$ is related to the electrostatic potential ψ by the relation $\mathbf{G} = \nabla_h \psi \times \hat{\mathbf{z}}$. Therefore $\mathbf{G}$ can be named an "electrostatic field". To find

a unique solution for the induction equation (3), therefore, one needs a unique solution for the electrostatic potential ψ or, equivalently, a unique solution for the electrostatic field $\mathbf{G}$.

Given the gauge conditions of equation (10), calculating $\mathbf{G}$ is equivalent to the vector potential calculation of Chae (2001) and it can be performed in Fourier space. Indeed, the solution for the electrostatic field $\mathbf{G}$ reads (see also Chae 2001)

$$
\begin{aligned}
G_x &= \mathcal{F}^{-1}[(ik_y/(k_x^2 + k_y^2))\mathcal{F}(C_z)] \\
G_y &= \mathcal{F}^{-1}[-(ik_x/(k_x^2 + k_y^2))\mathcal{F}(C_z)] \quad ,
\end{aligned}
\tag{11}
$$

where $\mathcal{F}(r)$, $\mathcal{F}^{-1}(r)$ are the direct and the inverse Fourier transform of r, respectively, and

$$
C_z = (\nabla \times \mathbf{G})_z \quad .
\tag{12}
$$

However, a major difference between our problem and Chae's (2001) is that C_z is unknown and hence equations (11) cannot be evaluated. If $u_{\perp_z}$ is known, however, $\mathbf{G}$ and C_z can be specified iteratively and self-consistently, in accordance with the gauge conditions of equations (10). In essence, we iteratively solve the system of the three equations (10) and (12) for the two unknown horizontal components of $\mathbf{G}$ and for C_z by using equations (11). The system is closed and has a unique solution for $\mathbf{G}$ and C_z and, by extension, a unique solution for ψ.

To illustrate how knowledge of $u_{\perp_z}$ is sufficient to calculate $\mathbf{G}$ and C_z, let $\mathbf{u}_\perp$ be the desired unique solution of the induction equation (3) and $u_{\perp_z}$ be its known vertical component. Then, from equation (5) one obtains

$$
\mathbf{u}_{\perp_\mathbf{h}} = \frac{1}{B_z}(u_{\perp_z}\mathbf{B_h} - \nabla_h\phi - \mathbf{G}) \quad ,
\tag{13}
$$

where we have introduced the definition $\mathbf{G} = \nabla_h\psi \times \hat{\mathbf{z}}$ in equation (5). Solving equation (13) for $\mathbf{G}$ and substituting $(\partial\phi/\partial x)$, $(\partial\phi/\partial y)$ with the components of $\mathbf{v}$ from equations (7), one further obtains

$$
\mathbf{G} = (u_{\perp_z} - v_z)\mathbf{B} + \mathbf{G}_\perp \quad ,
\tag{14}
$$

where $\mathbf{G}_\perp = -B_z(\mathbf{u}_\perp - \mathbf{v})$. Obviously, $\mathbf{G}_\perp$ is a purely cross-field electrostatic field since $\mathbf{u}_\perp \perp \mathbf{B}$ and $\mathbf{v} \perp \mathbf{B}$. The field-aligned component of $\mathbf{G}$ in equation (14) is fully known since $u_{\perp_z}$, v_z, and $\mathbf{B}$ are known. If $\mathbf{G}_\perp$ is not accurately known, however, i.e. if $\mathbf{G}_\perp \cdot \mathbf{B} \neq 0$, then the associated error is given by the quantity $\Delta E = \mathbf{G}_\perp \cdot \mathbf{B}$ or, equivalently,

$$
\Delta E = \mathbf{G} \cdot \mathbf{B} - (u_{\perp_z} - v_z)B^2 \quad .
\tag{15}
$$

One may then introduce a correction $\delta\mathbf{G}$ to the electrostatic field $\mathbf{G}$, namely,

$$
\mathbf{G}' = \mathbf{G} + \delta\mathbf{G} \quad ,
\tag{16}
$$

such that $\mathbf{G}'_\perp \cdot \mathbf{B} = 0$, where $\mathbf{G}'_\perp = \mathbf{G}' - (u_{\perp_z} - v_z)\mathbf{B}$. This obviously implies that $\delta\mathbf{G} \cdot \mathbf{B} = -\Delta E$. A general form for $\delta\mathbf{G}$ would then be

$$\delta\mathbf{G} = -\Delta E\left(\frac{1}{k_1 B_x}, \frac{1}{k_2 B_y}, 0\right) \; ; \quad \frac{1}{k_1} + \frac{1}{k_2} = 1 \; , \tag{17}$$

where k_1, k_2 are real numbers. Assuming that $\delta\mathbf{G}$ has the minimum possible magnitude so that the correction from $\mathbf{G}$ to $\mathbf{G}'$ is the minimum possible, we can calculate k_1, k_2 and express $\delta\mathbf{G}$ as follows:

$$\delta\mathbf{G} = -\frac{\Delta E}{B_h^2}(B_x, B_y, 0) \; . \tag{18}$$

Based on the above considerations, we can now calculate iteratively an electrostatic field $\mathbf{G}$ that satisfies both the gauge conditions of equation (10) and the orthogonality condition $\mathbf{G}_\perp \cdot \mathbf{B} = 0$ for its cross-field component $\mathbf{G}_\perp$. The devised iterative scheme is as follows:

(I) At iteration 0, use $\mathbf{G}^{(0)} = (u_{\perp_z} - v_z)\mathbf{B_h} + \mathbf{v_h}B_z$ as a first guess for $\mathbf{G}$
(from equation (14) assuming than $\mathbf{u}_{\perp_\mathbf{h}} = 0$ in $\mathbf{G}_\perp$)

....

(II) At iteration n ($n = 0, 1, 2, ...$), calculate $C_z^{(n)} = (\nabla \times \mathbf{G}^{(n)})_z$

(III) At iteration $n + 1/2$, evaluate equations (11) for $\mathbf{G}^{(n+1/2)}$
(thus solving equation (12) while enforcing the gauge conditions of equation (10))

(IV) At iteration $n + 1/2$, calculate the correction $\delta\mathbf{G}^{(n+1/2)}$ of $\mathbf{G}^{(n+1/2)}$ from equations (15) and (18)

(V) At iteration $n + 1$, update $\mathbf{G}^{(n+1)} = \mathbf{G}^{(n+1/2)} + \delta\mathbf{G}^{(n+1/2)}$ and continue from step II, etc.

Because we demand that $\delta\mathbf{G}$ has the minimum possible magnitude, $\delta G = |\Delta E|$, which decreases with each iteration, the above scheme converges asymptotically to a solution for the electrostatic field $\mathbf{G}$ with correction $\delta\mathbf{G} \to 0$. Convergence at iteration n is checked by means of a normalized dimensionless ratio $\mathcal{R}$ of the form

$$\mathcal{R} = \frac{\sum(|G_x^{(n)} - G_x^{(n-1)}| + |G_y^{(n)} - G_y^{(n-1)}|)}{\sum(|G_x^{(n)}| + |G_x^{(n-1)}| + |G_y^{(n)}| + |G_y^{(n-1)}|)} \; , \tag{19}$$

or, alternatively,

$$\mathcal{R} = \frac{\sum(|\mathbf{G}^{(n)} - \mathbf{G}^{(n-1)}|)}{\sum(|\mathbf{G}^{(n)}| + |\mathbf{G}^{(n-1)}|)} \; , \tag{20}$$

where the summation includes only locations with well-measured magnetic flux, i.e., locations where the vertical and the horizontal magnetic field components are larger than their associated uncertainties. Because we use discrete Fourier transforms the above calculations are somewhat approximate, so $\mathcal{R} = 0$ is achieved with respect to a prescribed fractional tolerance limit ε_c. Either form of $\mathcal{R}$ (equations (19), (20)) leads to the same results. The process stops at iteration n if the fraction

$$\varepsilon = \frac{|\mathcal{R}^{(n)} - \mathcal{R}^{(n-1)}|}{\mathcal{R}^{(n)} + \mathcal{R}^{(n-1)}} < \varepsilon_c \quad . \tag{21}$$

In the examples of §5 we have used $\varepsilon_c = 10^{-4}$.

After its calculation, we can use the electrostatic field $\mathbf{G}$ in equation (13) to calculate the horizontal inductive cross-field velocity $\mathbf{u}_{\perp_\mathbf{h}}$. The vertical component $u_{\perp_z}$ is *a priori* known, so one obtains a unique solution of the induction equation (3) for the cross-field velocity $\mathbf{u}_\perp$. Notice that the above formalism to infer $\mathbf{G}$ can be modified accordingly if $u_{\perp_x}$ or $u_{\perp_y}$, rather than $u_{\perp_z}$, are assumed known.

2.2. Field-aligned velocity: rotation of the Doppler velocity

Besides the cross-field velocity $\mathbf{u}_\perp$ one also needs the field-aligned velocity $\mathbf{u}_\parallel$ to fully reconstruct the inductive velocity field $\mathbf{u} = \mathbf{u}_\perp + \mathbf{u}_\parallel$. The field-aligned velocity cannot be treated by the induction equation and therefore its calculation requires additional information or assumptions. In the formulation of §2.1 the vertical cross-field velocity $u_{\perp_z}$ is assumed known but the vertical field-aligned velocity $u_{\parallel_z}$ and the total vertical velocity $u_z = u_{\parallel_z} + u_{\perp_z}$ are unknown. Evidently, if either $u_{\parallel_z}$ or u_z are known together with $u_{\perp_z}$, the field-aligned velocity $\mathbf{u}_\parallel$ can be calculated by the relation

$$\mathbf{u}_\parallel = \frac{u_{\parallel_z}}{B_z}\mathbf{B} = \frac{u_z - u_{\perp_z}}{B_z}\mathbf{B} \quad . \tag{22}$$

Therefore, the problem of calculating the field-aligned flows is essentially a problem of calculating $u_{\parallel_z}$ or u_z for a given $u_{\perp_z}$. To calculate u_z we use the longitudinal Doppler velocity u_l, available for nearly any vector magnetogram measurement of a given active region. From the geometrical transformation to the heliographic reference system (Gary & Hagyard 1990) the longitudinal velocity u_l and the heliographic components u_x, u_y, u_z of the velocity field vector $\mathbf{u}$ on the observer's (image) plane are related as follows:

$$u_l = \alpha u_x + \beta u_y + \gamma u_z \quad , \tag{23}$$

where α, β, γ are the direction cosines of the transformation. Their values can be calculated at each location of the image plane by means of this location's heliographic latitude and

longitude, the heliographic latitude and longitude of the center of the solar disk, and the angular position of the northern extremity of the solar rotation axis, measured eastward from the northernmost point of the solar disk (solar P-angle). Decomposing the velocity components u_i; $i \equiv \{x, y, z\}$, into a field-aligned and a cross-field terms, $u_{\|_i}$ and $u_{\perp_i}$, respectively, equation (23) can be solved for u_z to give

$$u_z = \frac{B_z}{B_l}(u_l - \alpha u_{\perp_x} - \beta u_{\perp_y} - \gamma u_{\perp_z}) + u_{\perp_z} \quad , \tag{24}$$

where $B_l = \alpha B_x + \beta B_y + \gamma B_z$ is the longitudinal magnetic field related to the heliographic magnetic field vector (B_x, B_y, B_z) by means of the direction cosines α, β, and γ. The first term in the rhs of equation (24) obviously corresponds to the field-aligned vertical velocity $u_{\|_z}$. Equation (24) suggests that the Doppler velocity u_l alone does not suffice for the calculation of the vertical velocity u_z and hence of the field-aligned flows. One also needs the cross-field velocity $\mathbf{u}_\perp$ obtained after solving the induction equation. On disk center, equation (24) directly implies $u_z = u_l$ since $B_z = B_l$ and $\alpha = \beta = 0$, while $\gamma = 1$.

Summarizing, we describe generally how an inductive velocity field $\mathbf{u}$ can be fully reconstructed from its field-aligned and cross-field components. The cross-field velocity $\mathbf{u}_\perp$ is obtained as a solution of the ideal induction equation, while the field-aligned velocity $\mathbf{u}_\|$ is calculated as shown in equation (24) using the Doppler velocity and the inferred cross-field velocity to obtain the vertical component u_z of $\mathbf{u}$ or the vertical component $u_{\|_z}$ of $\mathbf{u}_\|$.

2.3. Algorithmic implementation

Given a pair of co-aligned vector magnetograms, $\mathbf{B_1}$ and $\mathbf{B_2}$, obtained at times t and $t + \Delta t$, respectively, we calculate the inductive cross-field velocity $\mathbf{u}_\perp$ and the field-aligned velocity $\mathbf{u}_\|$ at time $t + (\Delta t/2)$ assuming that this velocity solution accounts for the evolution of the vertical magnetic field observed between t and $t + \Delta t$. The velocity solution corresponds to an average magnetic field $\mathbf{B} = (1/2)(\mathbf{B_1} + \mathbf{B_2})$ and an average Doppler velocity $u_l = (1/2)(u_{l_1} + u_{l_2})$, where u_{l_1}, u_{l_2} are the Doppler velocities corresponding to the magnetograms $\mathbf{B_1}$, $\mathbf{B_2}$, respectively. The above averages are assumed to describe the magnetic configuration at time $t + (\Delta t/2)$. From these assumptions the temporal derivative $(\partial B_z / \partial t)$ in the induction equation (3) can be approximated by a finite difference between B_{1_z} and B_{2_z}, namely,

$$\frac{\Delta B_z}{\Delta t} \simeq \frac{1}{\Delta t}(B_{2_z} - B_{1_z}) \quad . \tag{25}$$

The horizontal derivatives $(\partial Q/\partial x)$, $(\partial Q/\partial y)$ of any quantity Q can also be approximated by central finite differences of the form

$$
\begin{aligned}
(\Delta Q/\Delta x) &= [1/(2\lambda)][Q(x+1,y) - Q(x-1,y)] \\
(\Delta Q/\Delta y) &= [1/(2\lambda)][Q(x,y+1) - Q(x,y-1)] \ ,
\end{aligned}
\tag{26}
$$

respectively, where λ is the linear size of the magnetogram's pixel.

As mentioned in §2.1.1, Poisson's equation (6) is solved for the stream function ϕ on the plane S of the magnetic field measurements assuming homogeneous Dirichlet boundary conditions equal to zero on ∂S. If the SOR algorithm is applied for this purpose then one also needs a spectral radius $\rho_{jac} = (1/2)[cos(\pi/L_1) + cos(\pi/L_2)]$ for the Jacobi relaxation, where a magnetogram with linear dimensions $L_1 \times L_2$ and a square pixel $(\lambda_x = \lambda_y = \lambda)$ is assumed. This selection is a special case of the general examples discussed by Press et al. (1992). To further expedite the SOR, the Chebyshev acceleration scheme may be used in the selection of the over-relaxation parameter ω, as also described by Press et al. (1992). In this study we use the faster, but more complicated, ADI algorithm. Since the ADI numerical scheme was originally introduced to solve the time-dependent "heat flow" equation $(\partial\phi/\partial t) - \eta\nabla^2\phi = \rho$ on a given plane, we use $\eta = 1$, a fixed $\rho = -(\partial B_z/\partial t)$, and $t \to \infty$ to reach Poisson's equation (6).

Both the SOR and the ADI algorithms can solve equation (6) with an accuracy restricted only by the machine accuracy for any given $(\Delta B_z/\Delta t)$. In the ILCT and MEF solutions both ϕ and ψ are obtained by solving Poisson's equations, so any given temporal variation $(\Delta B_z/\Delta t)$ is reproduced up to machine accuracy for non-zero ψ. This is not the case for our general technique, where the electrostatic field $\mathbf{G}$, and hence the electrostatic potential ψ, are calculated within a reasonable error. The error stems from the convergence process in minimizing the dimensionless ratio $\mathcal{R}$ (equations (19), (20)) because of the use of the approximate Fourier transforms. Nevertheless, this error is not large enough to inflict a serious impact in the calculation of $\mathbf{u}_\perp$. As we will see in the examples of §5 the error in the minimization of $\mathcal{R}$ is smaller than $\sim 7\%$ in all cases. Numerical tests have shown that the error decreases substantially when the quality and continuity of the magnetic field measurements improves, i.e., when the noise decreases and the smoothness of the magnetic field structure increases. For tested synthetic magnetograms free of observational noise (Abbett 2005, private communication), for example, the error in $\mathcal{R} \simeq 0$ is typically less than 1%.

3. Analytical expressions for the velocity field

In this Section we provide general analytical expressions for the velocity field $\mathbf{u}$ acting on a given magnetic configuration $\mathbf{B}$. In connection with the previous sections, we assume that $\mathbf{B}$ is the average of two magnetic configurations, $\mathbf{B_1}$ and $\mathbf{B_2}$, obtained at times t and $t + \Delta t$, respectively. We will derive both the field-aligned and the cross-field components of $\mathbf{u}$.

We begin by considering Ampére's law in conjunction with the simplified Ohm's law for the electric current density $\mathbf{J}$: from Ampére's law, $\mathbf{J} = (c/4\pi)\nabla \times \mathbf{B}$, replace $\mathbf{B}$ by $B\hat{\mathbf{b}}$ to obtain

$$\mathbf{J} = \mathbf{J_1} + \mathbf{J_2} , \quad where \quad \mathbf{J_1} = \frac{cB}{4\pi}\nabla \times \hat{\mathbf{b}} \quad and \quad \mathbf{J_2} = \frac{c}{4\pi}\nabla B \times \hat{\mathbf{b}} , \tag{27}$$

where $\hat{\mathbf{b}}$ is the unit vector along the magnetic field lines. From equation (27) we notice that $\mathbf{J_2}$ is a purely cross-field component of the current density $\mathbf{J}$ while $\mathbf{J_1}$ includes, in general, a field-aligned and a cross-field component.

From the simplified Ohm's law, on the other hand, one obtains

$$\mathbf{J} = \mathbf{J'_1} + \mathbf{J'_2} , \quad where \quad \mathbf{J'_1} = \sigma\mathbf{E} \quad and \quad \mathbf{J'_2} = \frac{\sigma}{c}\mathbf{u} \times \mathbf{B} , \tag{28}$$

where σ is the electrical conductivity and $\mathbf{E}$ is the electric field acting on the plasma at rest. We notice that $\mathbf{J'_2} \perp \hat{\mathbf{b}}$ while $\mathbf{J'_1}$ generally includes a field-aligned and a cross-field component.

Both $\mathbf{J_2}$ and $\mathbf{J'_2}$ lie fully on the plane $S_\perp$ perpendicular to the magnetic field vector $\hat{\mathbf{b}}$ at any given spatial location. Therefore, there is a current density $\mathbf{J_\perp}$ also lying on $S_\perp$ such that

$$\mathbf{J'_2} = \mathbf{J_2} + \mathbf{J_\perp} . \tag{29}$$

Substituting $\mathbf{J'_2}$ from equation (28) into equation (29), one finds

$$\mathbf{u} \times \hat{\mathbf{b}} = \frac{\eta}{B}\mathbf{j_2} + \frac{\eta}{B}\mathbf{j_\perp} , \tag{30}$$

where $\eta = (c^2/4\pi\sigma)$ is the magnetic diffusivity, $\mathbf{j_2} = (4\pi/c)\mathbf{J_2}$, and $\mathbf{j_\perp} = (4\pi/c)\mathbf{J_\perp}$. From equation (30) one may now infer the horizontal components u_x, u_y of $\mathbf{u}$, namely,

$$\begin{aligned} u_x &= (1/b_z)[u_z b_x - (\eta/B)j_{2_y} - (\eta/B)j_{\perp_y}] \\ u_y &= (1/b_z)[u_z b_y + (\eta/B)j_{2_x} + (\eta/B)j_{\perp_x}] , \end{aligned} \tag{31}$$

where $b_i = (B_i/B)$; $i \equiv \{x, y, z\}$ are the relative magnetic field strengths and the components of $\hat{\mathbf{b}}$. An important point regarding equation (30) and its solution, equations (31), is that

one of the components of the velocity $\mathbf{u}$, in the above formulation the vertical velocity u_z, is left fully *unconstrained.* Moreover, all the components of $\mathbf{j}_\perp$, the horizontal components of $\mathbf{j_2}$ (see also equation (27)), and the magnetic diffusivity η are unknown. Evidently, therefore, $\mathbf{u}$ cannot be evaluated by equations (31). Nevertheless, one may further decompose $\mathbf{u}$ into a field-aligned and a cross-field components, $\mathbf{u}_{||}$ and $\mathbf{u}_\perp$, respectively. First, we multiply equation (30) externally by $\hat{\mathbf{b}}$ to solve for the cross-field velocity, namely,

$$\mathbf{u}_\perp = -\frac{\eta}{B}\mathbf{j_2} \times \hat{\mathbf{b}} - \frac{\eta}{B}\mathbf{j}_\perp \times \hat{\mathbf{b}} \ , \tag{32}$$

or, by substituting equation (27) for $\mathbf{j_2}$,

$$\mathbf{u}_\perp = \frac{\eta}{B}(\nabla B)_\perp - \frac{\eta}{B}\mathbf{j}_\perp \times \hat{\mathbf{b}} \ , \tag{33}$$

where $(\nabla B)_\perp$ is the cross-field component of ∇B. Now we can use equations (31) and the definition of the field-aligned velocity, $\mathbf{u}_{||} = (\mathbf{u} \cdot \hat{\mathbf{b}})\hat{\mathbf{b}}$, to obtain

$$\mathbf{u}_{||} = [(u_z - u_{\perp_z})/b_z]\hat{\mathbf{b}} \ , \tag{34}$$

where we have used the vertical component of the vector equation (32).

While we cannot directly evaluate $\mathbf{u}_{||}$ and $\mathbf{u}_\perp$ from equations (32) - (34), the above expressions are useful because they provide clues on a particular prescription for $u_{\perp_z}$ that will be used to enforce a unique solution of the ideal induction equation.

The general equations (32) and (33) may give the impression that $\mathbf{u}_\perp = 0$ in the ideal MHD limit, where $\eta \to 0$. This is not the case, however: $\mathbf{j}_\perp$ from equations (28) and (29) scales linearly with the electrical conductivity σ, i.e., $j_\perp \propto \sigma \propto (1/\eta)$. Therefore, $\lim_{\eta \to 0} u_\perp \propto \lim_{\eta \to 0}(\eta/\eta)$, which does not necessarily vanish.

4. Minimum structure velocity field reconstruction

4.1. The cross-field MSR velocity

As noted in §3, the analytical expressions for the field-aligned and the cross-field velocity components, equations (32) - (34), cannot be evaluated in their present form. As a first step to evaluate them, let us employ an assumption regarding $\mathbf{u}_\perp$, ∇B, and $\hat{\mathbf{b}}$: we assume that the cross-field velocity $\mathbf{u}_\perp$, equation (33), relates *only* to the cross-field magnetic gradients $(\nabla B)_\perp$ and aims to either sustain or eliminate them. In other words, we assume that $\mathbf{u}_\perp$ lies on the plane defined by $(\nabla B)_\perp$ and $\hat{\mathbf{b}}$ at any given *strong-field* location. This assumption is not intended for weakly or partially magnetized regions and yields the mathematical relation

$$\nabla B \times \hat{\mathbf{b}} \cdot \mathbf{u} = 0 \ \ or, \ \ equivalently, \ \ \ (\nabla B)_\perp \times \hat{\mathbf{b}} \cdot \mathbf{u}_\perp = 0 \ , \tag{35}$$

since only the cross-field components $(\nabla B)_\perp$ and $\mathbf{u}_\perp$ of ∇B and $\mathbf{u}$, respectively, participate in the equation. Correlating the two cross-field current density components $\mathbf{J_2}$ and $\mathbf{J'_2}$ from equations (27) and (28), respectively, one finds

$$\mathbf{J_2} \times \mathbf{J'_2} = -\frac{\sigma}{4\pi}(\nabla B \times \hat{\mathbf{b}} \cdot \mathbf{u})\mathbf{B} \ . \tag{36}$$

From our assumption in equation (35) one then finds $\mathbf{J_2} \times \mathbf{J'_2} = 0$, so $\mathbf{J'_2} = k\mathbf{J_2}$, where k is a real number. From equation (29) one further finds $\mathbf{j}_\perp = (k-1)\mathbf{j_2}$ and the cross-field velocity $\mathbf{u}_\perp$ from the general equations (32) or (33) becomes

$$\mathbf{u}_\perp = -\frac{\eta}{B}k\mathbf{j_2} \times \hat{\mathbf{b}} \quad or \quad \mathbf{u}_\perp = \frac{\eta}{B}k(\nabla B)_\perp \ , \tag{37}$$

respectively.

Despite the above simplification furnished by the assumed *coplanarity* between $\mathbf{u}_\perp$, $(\nabla B)_\perp$, and $\hat{\mathbf{b}}$, equations (37) still cannot be evaluated. Therefore, we will further employ the *minimum structure* approximation. This approximation has been introduced and discussed extensively by Georgoulis, LaBonte, & Metcalf (2004) and Georgoulis & LaBonte (2004). The idea behind the minimum structure assumption is to minimize the sheath currents that are thought to flow peripherally on the surfaces of magnetic flux tubes in the low solar atmosphere, thus making the low-lying magnetic fields as *space-filling* as possible. More specifically, the minimum structure approximation minimizes the magnitude J_2 of the cross-field current density $\mathbf{J_2}$ in equation (27) by solving for the unknown vertical gradient $(\partial B/\partial z)$ of the magnetic field strength. To realize that this is consistent with minimizing the surface "sheath" currents, consider a magnetic flux tube of finite cross-section embedded in a field-free atmosphere. Then, unless ∇B is fully field-aligned, J_2 is more intense on the surface of the flux tube, where the transition from a magnetized into an unmagnetized medium takes place. The magnitude J_2 of $\mathbf{J_2}$ becomes minimum when

$$\frac{\partial B}{\partial z} = \frac{b_z}{b_x^2 + b_y^2}(b_x\frac{\partial B}{\partial x} + b_y\frac{\partial B}{\partial y}) \ . \tag{38}$$

Knowledge of $(\partial B/\partial z)$ enables one to calculate the components of $\mathbf{J_2}$ or $\mathbf{j_2} = (4\pi/c)\mathbf{J_2}$ from equation (27). Substituting $(\partial B/\partial z)$ from equation (38) in the definition of $\mathbf{J_2}$, equation (27), one finds that the minimum structure approximation leads to

$$(\mathbf{j_2} \times \hat{\mathbf{b}})_z = 0 \quad or, \ equivalently, \quad (\nabla B)_{\perp_z} = 0 \ . \tag{39}$$

Substituting equations (39) of the minimum structure approximation into equations (37) of the coplanarity assumption one then finds that the vertical component $u_{\perp_z}$ of the cross-field velocity becomes zero, i.e.,

$$u_{\perp_z} = 0 \ . \tag{40}$$

Therefore, a restricted *coplanar* minimum structure approximation results in a purely horizontal cross-field velocity $\mathbf{u}_\perp$. Both the minimum structure approximation and the coplanarity assumption are intended for strongly magnetized regions and hence they can be combined. Notice, however, that the assumption $u_{\perp_z} = 0$ is principally *inconsistent* with magnetic flux emergence or submergence, because these effects take place along polarity reversal lines, where $B_z = 0$, so $u_{\perp_z}$ has to be nonzero by definition in these locations. We believe that our approximation can be justified, however, if one considers the length and time scales involved in flux emergence or submergence. These issues are discussed in detail in §6.1, but in summary the effects of flux emergence/submergence generally require length scales much smaller and time scales much larger than the respective scales of interest in an inductive velocity field calculation. Nonetheless, the coplanar minimum structure approximation is expected to perform poorly in small-scale magnetic features characterized by significant flux emergence or submergence.

One might think that the coplanarity assumption, equation (35), provides an additional constraint for $u_{\perp_z}$, besides equation (40). This would invalidate our coplanar minimum structure approximation since the system of equations would then become overdetermined (equations (3), (40), $\mathbf{u}_\perp \cdot \mathbf{B} = 0$, and equation (35) for the three components of $\mathbf{u}_\perp$). This is not the case, however: the coplanarity assumption, equation (35), combined with the orthogonality condition, $\mathbf{u}_\perp \cdot \mathbf{B} = 0$, can only give $u_{\perp_z} = 0$ in the minimum structure approximation. To realize this, one may write equation (35) as follows:

$$ u_{\perp_z} = -\frac{1}{(\nabla B \times \mathbf{B})_z} [u_{\perp_x}(\nabla B \times \mathbf{B})_x + u_{\perp_y}(\nabla B \times \mathbf{B})_y] \ . \tag{41} $$

Substituting equation (38) of the minimum structure assumption into equation (41) one finds

$$ u_{\perp_z} = \frac{B_z}{B_h^2} \mathbf{B}_h \cdot \mathbf{u}_{\perp_h} \ . \tag{42} $$

Now, from the orthogonality condition between $\mathbf{u}_\perp$ and $\mathbf{B}$ one obtains

$$ u_{\perp_z} = -\frac{1}{B_z} \mathbf{B}_h \cdot \mathbf{u}_{\perp_h} \ . \tag{43} $$

Combining equations (42) and (43) for nonzero B_z and $\mathbf{B_h}$, one finds

$$ B_z^2 \mathbf{B}_h \cdot \mathbf{u}_{\perp_h} = -B_h^2 \mathbf{B}_h \cdot \mathbf{u}_{\perp_h} \ , \tag{44} $$

which is only true if $\mathbf{B}_h \cdot \mathbf{u}_{\perp_h} = 0$. The only case where this is valid is when $u_{\perp_z} = 0$, as readily shown from equations (42) and (43). Therefore, the coplanar minimum structure assumption closes the system of equations for $\mathbf{u}_\perp$ which can now be solved exactly and uniquely.

4.2. The field-aligned MSR velocity

Using our special case of a coplanar minimum structure approximation, $u_{\perp_z} = 0$, the vertical velocity u_z from equation (24) simplifies to

$$u_z = \frac{B_z}{B_l}(u_l - \alpha u_{\perp_x} - \beta u_{\perp_y}) \ . \tag{45}$$

Equation (45) will be used in the following to calculate the field-aligned velocity $\mathbf{u}_{||}$ in the coplanar minimum structure approximation by means of equation (34).

5. Reconstruction of the MSR velocity field in solar active regions

To calculate the MSR velocity field vector in solar active regions we will use vector magnetogram data obtained by the Imaging Vector Magnetograph (IVM; Mickey et al. 1996) of the University of Hawaii's Mees Solar Observatory. The IVM records the complete Stokes vector at each of 30 spectral points through the Fe I 6302.5 Å photospheric spectral line. The magnetic field components are obtained via an inversion code that includes LTE radiative transfer, magneto-optic effects, and the filling factor of the unresolved flux tubes (Landolfi & degl'Innocenti 1982).

The above inversion code also determines the Doppler shift of the spectral line, and hence the longitudinal Doppler velocity. The fit to the Stokes I profile determines the line-center wavelength of the Fe I line with velocity V_I. The fit to the Stokes Q, U, and V profiles for the magnetic field components determines the velocity V_m of the magnetized areas and provides the wavelength difference from the Stokes I solution with velocity $\Delta V_m = V_m - V_I$. The longitudinal velocity u_l is then calculated by the relation

$$u_l = V_I + \Delta V_m \ . \tag{46}$$

The instrumental spatial quadratic variation of wavelength, caused by the off-axis passage through the Fabry-Perot etalon, is removed at the end. Equation (46) provides the correct Doppler velocity for magnetized areas and accounts for the potential error described by Chae, Moon, & Pevtsov (2004) where using the shift V_I of Stokes I at line center risks mixing the HD longitudinal motions of the unmagnetized plasma with the MHD motions of the magnetized plasma. Nevertheless, there is still space for improvement for the IVM Doppler velocities because an error in the reduction of the magnetograms tends to weigh ΔV_m by the filling factor f. As a result, ΔV_m in equation (46) corresponds more to $f\Delta V_m$. The effect is minimal in our calculations since we focus on strong-field regions such as sunspots and strong-field plages, where $f \simeq 1$, but it needs to be addressed in any case. In addition, we average the

inferred Stokes images for timescales of 20 min to 30 min to eliminate oscillatory effects, such as the $5 - min$ oscillations, from the inferred Doppler velocity u_l.

The 180°-ambiguity for each magnetogram of a given pair has been resolved using the structure minimization technique of Georgoulis, LaBonte, & Metcalf (2004). After the ambiguity is resolved the magnetograms are co-aligned with respect to their vertical components. Besides eliminating oscillatory effects in the Doppler velocity, averaging over periods of $20 - 30$ min enhances the signal-to-noise ratio in both the inferred magnetic field components and the longitudinal velocity. We use noise thresholds of 100 G and 200 G for the averaged vertical and horizontal magnetic fields, respectively. The calculations described in §§2 and 4 are performed using the heliographic magnetic field components on the image plane, but the results can be readily transferred to the local, heliographic, plane. In the following, we discuss three examples of active regions (ARs) that showed distinctive flows.

5.1. NOAA AR 9114

A series of vector magnetograms of NOAA AR 9114 were recorded by the IVM on 2000 August 8. Figure 1 shows the average ambiguity-free magnetic field vector (Figure 1a) and Doppler velocity (Figure 1b) for a pair of vector magnetograms obtained at 19:31 UT and at 19:59 UT.

In Figure 2 we illustrate the convergence process in calculating electrostatic field $\mathbf{G}$. As discussed in §2.3, the use of Fourier transforms does not provide results with accuracy up to the machine accuracy, unlike the ADI or SOR techniques. In Figure 2 the error in minimizing $\mathcal{R}$ ($\mathcal{R} \simeq 0$) is $\sim 7\%$ because $\mathbf{B}$ is somewhat noisy, despite the averaging.

Given the approximate calculation of the cross-field velocity $\mathbf{u}_\perp$, it is interesting to compare the observed temporal variation ($\Delta B_z/\Delta t$) of the vertical magnetic field B_z between the two magnetograms with the reproduced temporal variation using the solution for $\mathbf{u}_\perp$. This can be done by advancing the average B_z in time for a time difference ($\Delta t/2$), using the velocity field $\mathbf{u}_\perp$ in the induction equation (3). Unfortunately, we cannot do the same for the horizontal components B_x, B_y of $\mathbf{B}$, since this requires knowledge of the unknown height derivatives $(\partial B_x/\partial z)$, $(\partial B_y/\partial z)$ besides $\mathbf{u}_\perp$. If these derivatives were known, one would then be able to advance the entire magnetogram from time $t + (\Delta t/2)$ to any reasonable time interval $\Delta t'$ and thus predict the temporal evolution of the magnetic field vector in compliance with the induction equation. The observed and the reproduced temporal variations $(\Delta B_z/\Delta t)$ are shown in Figures 3a and 3b, respectively. Notice that the observed $(\Delta B_z/\Delta t)$ is reproduced in remarkable detail, although a careful inspection will reveal that the ob-

served variation is noisier than the reproduced variation. This should be expected from the use of Fourier transforms. A correlation between the observed and the reproduced temporal variation is shown in Figure 3c. The correlation coefficient between the two quantities is ~ 0.95 for both the linear and the non-parametric (Spearman) rank estimations. The best linear fit to the scatter plot, indicated by the dashed line, shows a slope 1.08 ± 0.01 and it is very similar to the theoretical relation $(\Delta B_z/\Delta t)_{observed} = (\Delta B_z/\Delta t)_{reproduced}$, shown by the solid line.

The error in the convergence process for $\mathbf{G}$ and hence in the final $\mathbf{u}_\perp$ is not large enough to significantly impact the results. For a moderate $(\Delta B_z/\Delta t)_{observed} = 0.1\ G\ s^{-1}$ the best linear fit of Figure 3c shows an expected $(\Delta B_z/\Delta t)_{reproduced} \simeq 0.092\ G\ s^{-1}$, while for a large $(\Delta B_z/\Delta t)_{observed} = 0.2\ G\ s^{-1}$ the expected reproduced value is $\sim 0.184\ G\ s^{-1}$. Therefore, the expected mean fractional error $(|(\Delta B_z/\Delta t)_{observed} - (\Delta B_z/\Delta t)_{reproduced}|/|(\Delta B_z/\Delta t)_{observed}|)$ is $\sim 8\%$, similar to the error in finding $\mathcal{R} \simeq 0$. The reproduced values are systematically slightly smaller than the observed values. Large observed $(\Delta B_z/\Delta t)$ may occur because of noise or errors in the magnetic field measurements, subtle inaccuracies in the co-alignment of the two magnetograms or changes in the seeing conditions in the course of the ground-based observations and hence they cannot be reproduced using Fourier transforms. Further testing the accuracy of the $\mathbf{u}_\perp$-solution we find that it is consistent with the coplanarity assumption, equation (37), with a mean fractional error $[|\mathbf{u}_\perp \cdot (\nabla B \times \mathbf{B})|/(u_\perp|\nabla B \times \mathbf{B}|)]$ of $\sim 6.2\%$.

NOAA AR 9114 was chosen for this study because of the distinctive flows observed around the AR's leading sunspot with positive magnetic polarity. This sunspot exhibited both a counterclockwise rotation during the observing interval (see also Brown et al. 2003) and intense flux-dispersing sunspot outflows characterized by the appearance and disappearance of numerous short-lived moving magnetic features (see Harvey & Harvey 1973; Nindos & Zirin 1998 for classical descriptions). It is interesting to check whether the rotation and outflows are reproduced by the MSR velocity solution. The solution is shown in Figure 4 with the horizontal velocity vector plotted on top of the average vertical magnetic field (Figure 4a) and the vertical MSR velocity (Figure 4b), i.e., the velocity $u_z = u_{||_z}$, since $u_{\perp_z} = 0$. Only areas of strong magnetic field are shown in the images. The dashed box in Figure 4a indicates the sub-region occupied by the sunspot. As we can see from Figure 4, the sunspot's rotation and radial outflows are reproduced nicely. Outflows occur with a velocity ranging between $0.4\ km\ s^{-1}$ and $1\ km\ s^{-1}$. The calculated vertical velocity reveals mostly upflows reaching up to $0.5\ km\ s^{-1}$.

In Figure 5 we focus on the sunspot of the AR. The MSR velocity field has been calculated for three different magnetogram pairs of the AR over a period of $\sim 4\ hr$. We show the cross-field velocity $\mathbf{u}_\perp$ (upper row of images) and the total velocity $\mathbf{u}$ (lower row

of images). In all images, the grayscale background is the vertical velocity u_z.

The counterclockwise rotation of the sunspot observed by Brown et al. (2003) and inferred from the IVM magnetogram movie is evidently reproduced by the cross-field velocity (Figures 5a to 5c). The rotation involves the outer penumbra of the sunspot, while the inner penumbra and/or the outer edge of the umbra show a weaker opposite (clockwise) rotation. This, opposite to the prevailing, sunspot rotation is more evident in Figure 5c. Moving progressively from Figure 5a to Figure 5c we notice that the counterclockwise rotation of the sunspot appears to subside with time.

While the cross-field velocity is responsible for the sunspot rotation in NOAA AR 9114, the sunspot outflows are contributed by the field-aligned velocity (Figures 5d to 5f). The outflows persist at the northern part of the sunspot, but they appear to subside at the southern part of the sunspot. It is not easy to visually determine from the magnetogram movie whether the outflows at the southern part weaken during the end of IVM daily observing interval, while we can see them clearly at the northern part, as the northward flows are more intense and systematic than the southward ones. In addition, we noticed that the seeing conditions deteriorate toward the end of the observing interval, so weaker flows are probably harder to pick up. From Figures 5e, 5f a change is also evident in the vertical component of the MSR velocity, as compared to Figure 5d. Upflows of the order 0.5 $km\ s^{-1}$ characterize the umbra and part of the penumbra until ∼18:00 UT. These upflows have decreased significantly at ∼20:00 UT and they continue to decrease at ∼22:00 UT.

In general, we find that the most distinctive flow features in NOAA AR 9114, namely the sunspot rotation and outflows, are believably reproduced by the MSR velocity field solution. Moreover, Figure 5 shows the consistency of our velocity solution between different pairs of vector magnetograms, given the uncertainties and a likely change in the seeing conditions toward the end of the IVM observing interval. The inferred sunspot rotation indicates that left-handed twist is injected in the active-region atmosphere via the emergence of a plasma-carrying helical magnetic structure. Smaller, concentric, toroidal structures with opposite chirality may also emerge simultaneously, as indicated by the weaker opposite rotation seen in the inner parts of the penumbra or in the outer umbra. On the other hand, the Evershed outflows of the upwelled plasma occur as a result of the dynamic pressure gradients built up during the emergence process. Because this plasma is mostly magnetized, outflows occur mainly along the emerging magnetic field lines so they are captured by the field-aligned velocity solution. Both the sunspot rotation and the outflows appear to weaken in the course of time, at least for the southern part of the sunspot. If this is not an artifact owning to the variable seeing conditions, a possible clue might be provided by the decreasing vertical upflow velocity, which indicates that the emergence of the helical magnetic structure and

the upwelling of the plasma gradually subside with time.

5.2. NOAA AR 8210

The passage of NOAA AR 8210 from the visible solar disk early in May 1998 resulted in a series of solar flares and at least one halo CME on 1998 May 2 (Warmuth et al. 2000; Pohjolainen et al. 2001; Sterling & Moore 2001). The AR is a well-studied subject from photosphere to corona (Thompson et al. 2000; Wang et al. 2002; Roussev et al. 2004) and a case subject for the Solar MURI Project (Fisher et al. 2003) because of its dynamical activity linked to a distinctive δ-sunspot photospheric magnetic configuration. Intense photospheric flows were also observed. As a result, NOAA AR 8210 was the subject of the velocity field calculation in the studies of Welsch et al. (2004) and Longcope (2004).

The IVM obtained a series of vector magnetograms of the AR on 1998 May 1. For a pair of these magnetograms, taken at 17:20 UT and at 17:52 UT, the average ambiguity-free magnetic field vector and the average Doppler velocity are given in Figures 6a and 6b, respectively. A complex δ-sunspot configuration in the AR is evident from Figure 6a. Inspecting the IVM magnetogram movie we notice counterclockwise motions in the strong positive-polarity field adjacent to the eastern part of the sunspot. The spot itself appeared to move clockwise along the polarity inversion line, which presumably helped accumulating a significant magnetic shear. The western and southwestern parts of the sunspot exhibited significant outflows, while a mixed picture of inflows and outflows occurred at the southeastern part of the sunspot. Moreover, there was some flux emergence northwest of the sunspot with a small negative-polarity pore emerging and moving rapidly to the southwest.

We calculated the MSR velocity for the above pair of magnetograms. In this example, the convergence to the unique minimum structure solution (i.e. $\mathcal{R} \simeq 0$; Figure 2 for the previous example) was achieved with an error of $\sim 4.7\%$. The observed and the reproduced temporal variation ($\Delta B_z / \Delta t$) are given in Figures 7a and 7b. Again we note that the observed variation is reproduced closely, although it is somewhat noisier than the reproduced variation. Correlating the observed and reconstructed temporal variations (Fig. 7c) we calculate a high correlation coefficient ranging between 0.97 and 0.98, while the best linear fit of the scatter plot (dashed line; slope 1.05±0.005) is very similar to the theoretical relation of equality between the two temporal variations (solid line). From the best fit we find that for a commonly observed vertical field variation of 0.1 G s^{-1} the expected reproduced variation is ~ 0.95 G s^{-1}, while for a large observed variation of 0.2 G s^{-1} the expected reproduced variation is ~ 0.19 G s^{-1}. As with NOAA AR 9114, the expected mean fractional error $(|(\Delta B_z / \Delta t)_{observed} - (\Delta B_z / \Delta t)_{reproduced}| / |(\Delta B_z / \Delta t)_{observed}|)$ is $\sim 5\%$, similar to the error in

$\mathcal{R} \simeq 0$. Moreover, the mean fractional error $[|\mathbf{u}_\perp \cdot (\nabla B \times \mathbf{B})|/(u_\perp|\nabla B \times \mathbf{B}|)]$ in the fulfillment of the coplanarity assumption is $\sim 5\%$.

The MSR velocity field solution for the δ-sunspot is shown in Figure 8. We show both the cross-field velocity solution $\mathbf{u}_\perp$ (Figures 8a, 8c) and the total calculated velocity $\mathbf{u}$ (Figures 8b, 8d). We notice that both the sunspot outflows and part of the counterclockwise motion, especially in the northern part of the positive-polarity arm east of the δ-sunspot, are nicely shown. Sunspot outflows occur with a velocity $\sim (0.5 - 0.8)$ km s^{-1}, while the positive flux accumulations at the east move with a velocity $\sim (0.2 - 0.5)$ km s^{-1}. Some velocity shear along the polarity inversion line can be also seen. Calculations on, or very close to, the line are not possible because $|B_z| \to 0$, so we can only calculate the flows at the vicinity of the line. We also notice some inflows with velocity $\sim (0.5 - 0.8)$ km s^{-1} at the southeastern part of the δ-sunspot. The MSR solution shows these motions as both outflows and inflows for different pairs of magnetograms. This is probably because the fine mixture of inflows and outflows inferred from the IVM magnetogram movie in this area may not be reproduced reliably by the MSR solution. The clockwise rotation of the δ-sunspot, also inferred from the $H\alpha$ observations of Warmuth et al. (2000), is not evident in the MSR velocity solution.

From a visual comparison of the MSR solution, the ILCT solution of Welsch et al. (2004), and the MEF solution of Longcope (2004) we find that the strong penumbral inflows and outflows seen in the IVM magnetogram movie are reproduced by the MSR velocity but they are not a conspicuous feature of the ILCT and MEF solutions. The counter-clockwise motions of the positive-polarity arm of the sunspot, however, appear more or less in all three solutions. In terms of the calculated flow amplitude, the MSR solution leads to larger horizontal flows than both the ILCT and the MEF solutions. The strongest flows for these solutions appear to be ~ 0.4 km s^{-1} and ~ 0.8 km s^{-1}, respectively, while our calculated flows can be as fast as $\sim (1 - 1.5)$ km s^{-1}. It is not clear whether the MSR approach overestimates or the ILCT and the MEF approaches underestimate the horizontal cross-field velocity. Assuming $u_{\perp_z} = 0$ in the MSR technique may introduce additional horizontal flows to solve the induction equation. On the other hand, the ILCT solution relies on an essentially smoothed LCT velocity and the MEF solution explicitly demands minimal flows, so these two solutions may underestimate the horizontal flows. Regarding the small emerging flux region at the northwest of the δ-sunspot, indicated by the white oval in Figure 8a, only the ILCT solution reproduces the intense flows to the southwest. The MEF solution does not include this part of the AR in the analysis, while the MSR solution cannot reproduce these flows. There are two reasons for this discrepancy: first, as explained in the Introduction, any inductive technique assisted by tracking is more likely to reproduce such flows which may in part be apparent flows, caused by the emergence of inclined magnetic structures. Second, the main assumption behind the MSR solution, $u_{\perp_z} = 0$, may break down locally in

emerging flux regions as mentioned in §4.1 and discussed in detail in §6.1.

In Figure 9 we show the MSR velocity in the δ-sunspot for three different magnetogram pairs of the AR. The upper row of images (Figures 9a - 9c) show the MSR horizontal velocity plotted on top of the vertical magnetic field. In the lower row of images the grayscale background is the vertical component of the MSR velocity. The three magnetogram pairs cover a period of $\sim 2.5\ hr$. The MSR velocity solutions are similar in all three cases: both the counterclockwise motion of the positive polarity arm at the east of the sunspot and the penumbral inflows/outflows are similarly reproduced in all images while the solution for the vertical velocity changes only slightly.

5.3. NOAA AR 10030

NOAA AR 10030 was also a flaring AR involving large amounts of magnetic flux in a complex multipolar magnetic configuration. The most important event associated with this AR was a X3 flare followed by a halo CME late on 2002 July 15. We have calculated the MSR velocity field in the AR for a pair of vector magnetograms recorded by the IVM at 19:50 UT and at 20:21 UT on 2002 July 15. Figure 10a depicts the average, ambiguity-free, vertical magnetic field for the magnetogram pair, while Figure 10b shows the average Doppler velocity. Inspecting the IVM magnetogram movie of the AR late on 2002 July 15, we notice (i) a possible clockwise rotation of the westernmost leading sunspot of the AR (ovals A1 and B1 in Figures 10a and 10b, respectively) and (ii) a highly sheared neutral line close to the trailing spot of the AR at the east (ovals A2 and B2 in Figures 10a and 10b, respectively). The sheared neutral line is also associated with an intense upflow/downflow pattern in the longitudinal Doppler velocity with flow amplitudes $(0.6 - 0.8)\ km\ s^{-1}$.

In Figure 11 we show the observed (Figure 11a) and the reproduced (Figure 11b) temporal variations of the vertical magnetic field for the magnetogram pair. The observed temporal variation is somewhat noisier than the reproduced one, as is the case in the previous examples. In this particular example the convergence to the MSR solution was achieved with an error of $\sim 6.1\%$ for $\mathcal{R} \simeq 0$. The observed and the reproduced temporal variations are correlated in the scatter plot of Figure 11c. Both the linear and the Spearman rank correlation coefficient are ~ 0.94 and the best linear fit (dashed line; slope 1.06 ± 0.008) is close to the theoretical expression of equality between the two temporal variations (solid line). The mean fractional error between $(\Delta B_z/\Delta t)_{observed}$ and $(\Delta B_z/\Delta t)_{reproduced}$ is $\sim 6\%$, while the mean fractional error in the fulfillment of the coplanarity assumption is $\sim 4.4\%$.

In Figure 12 we depict the MSR velocity solution for the AR. The horizontal velocity is

plotted on top of B_z (Figure 12a) and on top of u_z (Figure 12b). Given the significant complexity of the magnetic configuration, individual features of the flow are hardly discernible. For this reason we focus on the two most conspicuous flow features of the IVM magnetogram movie, namely the clockwise rotation of the westernmost leading sunspot and the sheared neutral line at the east. The two corresponding sub-areas of the MSR velocity solution of Figure 12 are magnified and shown in details (A1), (B1) (sunspot) and (A2), (B2) (neutral line) in Figure 12. The clockwise rotation of the sunspot is evidently verified by the MSR velocity solution: the sunspot rotates with a velocity $\sim (0.3 - 0.6)\ km\ s^{-1}$. On the other hand, the MSR velocity solution reproduces part of the velocity shear at the vicinity of the neutral line but it does not show a fully sheared neutral line as one concludes from the magnetogram movie. As already mentioned, calculations on, or very close to, the neutral line are not possible because $|B_z| \to 0$. Shearing motions occur with a velocity $\sim (0.4 - 0.9)\ km\ s^{-1}$. In accordance with the Doppler velocity, the MSR vertical velocity also shows intense upflows/downflows with an amplitude of $\sim (0.7 - 0.8)\ km\ s^{-1}$. Summarizing, the MSR velocity reproduces reasonably the most characteristic flows in the AR.

The inductive velocity can give rise to additional information besides being utilized for 3D MHD simulations or for helicity flux calculations. For instance, one may partially calculate the *vorticity* $\zeta = \nabla \times \mathbf{u}$ associated with the flow. Just like the electric current density, only the vertical component of the vorticity, i.e., $\zeta_z = [(\partial u_y/\partial x) - (\partial u_x/\partial y)]$, can be calculated for single-height magnetic field observations and the respective velocity field vector. Even this limited vorticity information, however, can provide some knowledge of the temporal evolution on the plane of the calculations. A consistent sign of vorticity over a magnetic feature indicates vortex motions and whirling flows, while different signs of vorticity indicate velocity shear. There are strong indications that vortex motions are present in the convection zone on in shallow sub-photospheric layers (Kosovichev 2002; López Fuentes et al. 2003), while it has been shown that Parker's twisting and braiding of the magnetic field lines above the photosphere can be achieved by small-scale photospheric vortex motions overshooting into the corona (Meytlis & Strauss 1993; Lionello et al. 1998). The vertical vorticity for NOAA AR 10030 is given in Figure 13. The leading sunspot in the west (oval (a)) is mostly characterized by a unique sign of vorticity ($\zeta_z < 0$) which indicates a clockwise rotation, as also shown in Figure 12. For the other sub-regions of the AR, indicated by ovals (b), (c), and (d), there is evidence for both signs of vorticity, so velocity shear is at work in these areas. The sheared neutral line discussed above is one of them, indicated by oval (d). It is well known that the magnetic complexity increases in sheared regions and the likelihood of a flare-triggering instability is high. Indeed, the origin location of the X3 flare that was triggered in the AR is an area of strong vortex motions and possible shear, indicated by oval (b) in Figure 13 (see Liu et al. (2003) and Gary & Moore (2004) for more detailed

discussions).

A complete description of the evolution in NOAA AR 10030 using the MSR velocity lies beyond the scope of this study. From this example, however, we illustrate both the importance of knowing the velocity field together with the magnetic field vectors in a complex AR and that the MSR velocity field solution is detailed enough to be used in further analyses.

6. Discussion and Conclusions

Several important tasks in solar physics, from the anelastic (non-force-free) 3D MHD modeling of the magnetic fields in the corona to the calculation of the magnetic helicity flux or the quantitative assessment of flow patterns and vortex motions in the solar photosphere/chromosphere require simultaneous, reliable, velocity field information besides the measured magnetic field vector. The measured LCT velocity alone is insufficient for the study of flows in solar active regions and bears little agreement with the time-dependent MHD equations. An almost unanimous consensus calls for a velocity field calculation in compliance with the MHD theory and, in particular, with the induction equation. To calculate an inductive velocity, however, one needs reliable *vector* magnetograms, contrary to the LCT velocity that requires either longitudinal magnetograms or continuum images. This fact restricts the applicability of the induction equation. In addition, single-height magnetic field measurements allow only a partial use of the induction equation which makes the calculation of the cross-field velocity an under-determined problem. Additional hypotheses are, therefore, required to enforce a unique solution of the ideal induction equation. Three previous inductive techniques (Kusano et al. 2002; Welsch et al. 2004; Longcope 2004) have so far addressed the problem, each relying on its own assumptions. None of the above techniques attempts to calculate the field-aligned velocity besides the cross-field velocity.

In this study we attempt to generalize the problem (i) by introducing a general solution formalism for the vertical component of the ideal induction equation, and (ii) by introducing a method to calculate the field-aligned flows using the available Doppler velocity information together with the solution of the induction equation. The first action allows the use of any additional constraint to uniquely solve the ideal induction equation. Therefore, a multitude of inductive velocity solutions can be realized by means of our general formalism. The second action allows a complete reconstruction of the velocity field vector that includes the field-aligned velocity, provided that the Doppler velocity has been processed adequately to eliminate known systematic errors and biases. To show the feasibility of our general approach we calculate a unique inductive velocity relying on our own additional constraint, which is a coplanar minimum structure approximation. We avoid using the LCT velocity and

we do not explicitly demand minimal flows, although we do not consider these assumptions unreasonable by any means. In §6.1 we discuss the physics of the coplanar minimum structure approximation and in §6.2 we summarize our results for the MSR velocity in the three studied solar active regions.

6.1. Feasibility of the coplanar minimum structure approximation

As discussed in §4.1 the MSR cross-field velocity $\mathbf{u}_\perp$ (i) relates only to the cross-field magnetic gradients $(\nabla B)_\perp$ (equation (37)), and (ii) lies on the horizontal plane. There is no additional constraint in the relation of $\mathbf{u}_\perp$ and $(\nabla B)_\perp$ so the cross-field velocity can either sustain ($k > 0$) or relax ($k < 0$) the cross-field magnetic gradients. Illustrative examples of both actions of the velocity field can be found (i) in supergranules observed within active regions, where the supergranular boundaries are sustained by persistent converging flows caused by flux emergence at the center of neighboring cells (see, e.g., Georgoulis et al. 2002; Bernasconi et al. 2002), and (ii) in sunspots, where strong inflows/outflows are seen in several cases (e.g. our results for NOAA ARs 9114 and 8210). The sunspot outflows are caused by pressure gradients and tend to disperse strong magnetic field gradients at the penumbral edges caused by the magnetic flux accumulation and the upwelling of magnetized plasma.

To determine whether our coplanar minimum structure approach is compatible with fundamental laws we consider the MHD momentum equation, where the Lorentz force has been decomposed into a magnetic pressure force $(1/(8\pi))\nabla B^2 = (1/(4\pi))B\nabla B$ and a magnetic tension force $(1/(4\pi))(\mathbf{B} \cdot \nabla)\mathbf{B}$ (e.g., Jackson 1962), i.e.

$$\frac{\partial \mathbf{u}}{\partial t} + (\mathbf{u} \cdot \nabla)\mathbf{u} = -\nabla P + \frac{1}{4\pi}(\mathbf{B} \cdot \nabla)\mathbf{B} - \frac{B}{4\pi}\nabla B + \rho\mathbf{g} \ , \qquad (47)$$

where P is the gas pressure, ρ is the mass density, and $\mathbf{g} = -g\hat{\mathbf{z}}$ is the gravitational acceleration. Viscous forces are ignored in equation (47) in line with our ideal MHD approach. We seek to determine whether the MSR flows that result from the coplanar minimum structure approximation can balance the magnetic and non-magnetic forces of equation (47) in any given case. The analysis is simplified if we introduce a moving orthonormal coordinate system with the local axes defined by $\hat{\mathbf{b}}$, $\hat{\mathbf{b}}_1 = [(\nabla B)_\perp/|(\nabla B)_\perp|]$, and $\hat{\mathbf{b}}_2 = \hat{\mathbf{b}} \times \hat{\mathbf{b}}_1$. Then the magnetic field vector, the magnetic gradients, and the velocity field vector in the coplanar minimum structure approximation can be written as

$$\mathbf{B} = B\hat{\mathbf{b}} \ , \quad \nabla B = (\nabla B \cdot \hat{\mathbf{b}})\hat{\mathbf{b}} + (\nabla B)_\perp\hat{\mathbf{b}}_1 \ , \quad and \quad \mathbf{u} = (\mathbf{u} \cdot \hat{\mathbf{b}})\hat{\mathbf{b}} + s(u_\perp)u_\perp\hat{\mathbf{b}}_1 \ , \quad (48)$$

respectively, where $s(u_\perp) = k/|k|$ (equation (37)). Now the MHD momentum equation can be decomposed in its three components along $\hat{\mathbf{b}}$, $\hat{\mathbf{b}}_1$, and $\hat{\mathbf{b}}_2$. It can be readily shown that

MSR flows can be generated or modified $((\partial \mathbf{u}/\partial t) \neq 0)$ by magnetic and non-magnetic forces acting along $\hat{\mathbf{b}}$ and $\hat{\mathbf{b}}_{\mathbf{1}}$ since all terms in equation (47) have, in principle, nonzero components along $\hat{\mathbf{b}}$ and $\hat{\mathbf{b}}_{\mathbf{1}}$. Along $\hat{\mathbf{b}}_{\mathbf{2}}$, however, the MSR flows do not have a component, so $(\partial \mathbf{u}/\partial t) = 0$. In this case, equation (47) becomes

$$(\mathbf{u} \cdot \nabla)\mathbf{u} \cdot \hat{\mathbf{b}}_{\mathbf{2}} = -\frac{\partial P}{\partial b_2} + \frac{1}{4\pi}(\mathbf{B} \cdot \nabla)\mathbf{B} \cdot \hat{\mathbf{b}}_{\mathbf{2}} - \rho g \hat{\mathbf{z}} \cdot \hat{\mathbf{b}}_{\mathbf{2}} \quad . \qquad (49)$$

Although $\mathbf{u}$, ∇B, and $\mathbf{B}$ do not have a component along $\hat{\mathbf{b}}_{\mathbf{2}}$ (equations (48)), the dynamic flow pressure $(\mathbf{u} \cdot \nabla)\mathbf{u}$ and the magnetic tension $(\mathbf{B} \cdot \nabla)\mathbf{B}$ have nonzero components along $\hat{\mathbf{b}}_{\mathbf{2}}$ due to curvature effects. As a result, the MSR flows give rise to pressure forces along the $\hat{\mathbf{b}}_{\mathbf{2}}$-direction but a velocity generation or change $(\partial \mathbf{u}/\partial t)$ along $\hat{\mathbf{b}}_{\mathbf{2}}$ due to magnetic and non-magnetic forces is not allowed because the coplanar minimum structure approximation precludes any cross-field flows $\mathbf{u}_\perp$ along $\hat{\mathbf{b}}_{\mathbf{2}}$. This is a limitation of the approximation, so the MSR flows are expected to suppress some of the actual inductive flows and hence generate some artificial (horizontal, by construction $[u_{\perp_z} = 0]$) cross-field flows to satisfy the ideal induction equation. The extent of the approximation $u_{\perp_z} = 0$ determines the magnitude of the artificially introduced horizontal flows. In essence, the MSR solution allows both field aligned-flows and some cross-field flows (along $\hat{\mathbf{b}}_{\mathbf{1}}$). For the MSR solution to be compatible with the MHD momentum equation in the direction of the suppressed cross-field flows (along $\hat{\mathbf{b}}_{\mathbf{2}}$) the dynamic flow pressure must balance external gas pressure gradients, magnetic tension, and gravity *in the absence* of actual MSR flows. As a result, equation (49) shows that the coplanar minimum structure approximation, although not incompatible with the MHD momentum equation, restricts its generality along $\hat{\mathbf{b}}_{\mathbf{2}}$.

Let us now discuss the extent of the approximation $u_{\perp_z} = 0$ and its apparent contradiction with magnetic flux emergence or submergence. Vertical cross-field flows take place along polarity reversal lines where $B_z = 0$, so $u_{\perp_z} \neq 0$ by definition in this case. Such flows are necessary for the emergence or submergence of magnetic flux in the solar atmosphere and have been studied by several authors (see, e.g., Strous et al. 1996; van Driel-Gesztelyi, Malherbe, & Démoulin 2000; Chae, Moon, & Pevtsov 2004). However, it is important to consider two aspects of flux injection (emergence or submergence) through the solar photosphere and their relation to an inductive technique such as the MSR. These aspects are the length and time scales involved in flux injection.

It is generally accepted that flux emergence takes place along the polarity reversal lines in emerging flux regions and in granular length scales, much smaller than the supergranular scales of the resulting active regions. Recent high-resolution observations (Bernasconi et al. 2002; Pariat et al. 2004, and others) complement our understanding and suggest that in granular scales the convective overshoot carries short undulatory emerging field lines to

the surface. Some of these lines are convex ($\mathbf{\Omega}$-shaped) and do not need resistive effects to emerge/submerge rapidly because the drainage of the dense, unmagnetized, photospheric plasma is effectively assisted by the field-line geometry. However, many magnetic field lines are concave ($\mathbf{U}$-shaped) because this dense plasma keeps their horizontal central part anchored in the photosphere while the more vertical edges of the line emerge in the atmosphere. The submergence of such $\mathbf{U}$-loops may also occur ideally, because of their geometry, but their complete emergence requires resistive instabilities such as the Rayleigh-Taylor instability (Parker 1966) which occurs at length scales of the order few Mm (Pariat et al. 2004), the Kelvin-Helmholtz instability (Diver, Brown, & Rust 1996; Bernasconi et al. 2002) at similar length scales, or a sudden reshaping caused by the intense magnetic tension force developed in these lines with small radii of curvature (e.g., Priest 1982). In essence, the average ratio $|u_{\perp_z}/u_{||_z}|$ is probably large (of the order, or larger than, unity) in granular length scales, but it may be smaller than unity in supergranular scales since (i) flux injection is not observed in supergranular scales and (ii) all the instabilities proposed for resistive flux emergence require length scales of the order few $arcsec$, much smaller than supergranular scales. Macroscopic (supergranular) scales, however, are the scales of interest in inductive velocity calculation techniques. This is probably why our MSR velocity reasonably reproduces a number of macroscopic flow patterns in the active regions of §5 but this this is also why it may perform poorly in small spatial scales. The pixel size of most modern vector magnetographs is of the order $1''$ or less ($0.55''$ for the IVM data used here) so the above-mentioned instability length scales and the subsequent small-scale dynamical activity are most probably resolved, at least partially.

On the other hand, the emergence time scales for active regions are of the order few, to several, days. In an inductive velocity calculation the discretization of the induction equation (3) requires the smallest possible time differences between two successive vector magnetograms. If the Doppler velocity is used, however, time scales of at least a few tens of min are necessary to average the Doppler signal and to eliminate high-frequency oscillatory effects. In balancing between the two requirements, an optimal time scale of the order $20-30$ min in measurements having a cadence of a few min would both allow the discretized induction equation to work acceptably and the Doppler velocity to be properly averaged. This time scale is so much smaller than emerging flux region time scales that in practice one assumes that the evolution seen between two successive vector magnetograms is dominated by induction flows with only minor contribution from flux injection (emergence or submergence).

From the above discussion it becomes rather clear that the ratio $|u_{\perp_z}/u_{||_z}|$ in the length and time scales of interest to an inductive velocity calculation is either smaller or much smaller than unity, but it may become larger or much larger than unity in the small spatial and temporal scales at work in case of rapid flux emergence or submergence. This is why

the MSR solution breaks down locally for, say, the small emerging pore in NOAA AR 8210 (§5.2) or the canceling magnetic features reported by Chae, Moon, & Pevtsov (2004). In the former case, the intense horizontal flows of the emerging structure are not reproduced. In the latter case, the significant downward $u_{\perp_z}$ cannot be reproduced by construction of the MSR solution. Furthermore, if these flux cancellations are caused by resistive effects, an ideal MHD technique is impossible to realistically capture the dynamics of the process.

It is interesting to examine the feedback provided by numerical simulation results of ideal flux emergence (Fan 2001; Magara & Longcope 2003; Magara 2004). In all studies, different geometries of the emerging magnetic field lines are simultaneously considered. In Fan (2001) a nearly horizontal line corresponding to the axis of the ascending flux tube never emerges fully from the photosphere although the upper part of the tube rises well above the photospheric plane. In Magara & Longcope (2003) and Magara (2004) nearly horizontal field lines eventually reach substantial heights. It is argued, however, that the emergence behavior depends critically on both the geometry of the line and its assumed internal structure. Nearly horizontal lines imply a weaker plasma drainage toward their footpoints, so the gravitational force is more effective in blocking the expansion of the line. The drainage is more intense close to the footpoints of the line, where the magnetic field is more vertical, and hence these parts of the line ascend faster than the central part where a dip eventually develops and more unmagnetized plasma is stably accumulated. Magara & Longcope (2003) and Magara (2004) argue that the mass accumulation in the dip eventually enhances the magnetic forces so that the line reshapes, probably reconnects, and eventually expands upward. In any case, the local apex(es) of any ascending or descending twisted magnetic field line are horizontal, so in these locations $u_{\perp_z} \neq 0$. In strongly curved field lines, however, these locations occupy small parts of the line so whether $u_{\perp_z} \neq 0$ might depend on the considered length scales, as discussed previously. The above modeling studies appear to show that the upward motion of a magnetic field line is slower if the line is horizontal and nearly untwisted as opposed to the faster upward motion of twisted magnetic field lines which are tangent to the photospheric plane only locally. In other words, these results may imply that the average $|u_{\perp_z}/u_{||_z}| \gtrsim 1$ in small scales, near the local apexes of the line, while $|u_{\perp_z}/u_{||_z}| < 1$ or $|u_{\perp_z}/u_{||_z}| \ll 1$ if averaged over the entire length of the line.

6.2.   Concluding remarks

All different inductive techniques must resort to an additional constraint in order to reach a unique solution of the under-determined ideal induction equation. The problem originates from our inability to measure the magnetic field vector in a succession of heights

in and above the photosphere. The velocity field solution will be unique in the ideal limit of the induction equation only when simultaneous multi-height (i.e. photospheric and chromospheric) magnetic field measurements become available. The problem is also intractable when the resistive term of the induction equation is considered, because the magnetic diffusivity η is unknown. Even if a reliable model of η was used, however, new numerical techniques would be required to solve the resistive induction equation, so an envisioned step from ideal to non-ideal inductive techniques is inherently nontrivial.

Some authors suggest that the additional constraint needed to uniquely determine the solution to the vertical component of the ideal induction equation is readily available and is the LCT velocity $\mathbf{v_{LCT}}$ combined with the geometrical conjecture of Démoulin & Berger (2003) (equation (1)). This additional information is fully exploited by the ILCT technique of Welsch et al. (2004). Nevertheless, we choose not to use $\mathbf{v_{LCT}}$ as it is currently measured for a number of reasons: the map of $\mathbf{v_{LCT}}$ is coarser than the input maps; $\mathbf{v_{LCT}}$ is not really consistent with the induction equation; $\mathbf{v_{LCT}}$ may incorporate HD flows of the field-free plasma; and $\mathbf{v_{LCT}}$ represents only part of the kinetic power of the magnetized plasma in an AR, determined by a single choice of the LCT's FWHM apodizing window. As a result, $\mathbf{v_{LCT}}$ is not unique. In the absence of a physical criterion for the selection of the above control parameter, it is not clear which prescription for $\mathbf{v_{LCT}}$ should be chosen. We feel that if this central problem of the preferred LCT length scale is somehow addressed in the future the $\mathbf{v_{LCT}}$-solution together with equation (1) might indeed be useful in constraining the induction equation.

Comparing the MSR results with the results of the ILCT and the MEF techniques for NOAA AR 8210, we find that (i) the MSR provides a rather more detailed velocity field solution, assisted also by the field-aligned velocity calculation, and (ii) the MSR velocity tends to be larger than the ILCT and MEF velocities. This may be because the assumption $u_{\perp_z} = 0$ in the MSR solution introduces additional horizontal flows (§6.1) and/or because the ILCT and MEF solutions rely on smoothed (from LCT) and explicitly minimal flows, respectively. This is an unclear point and needs to be addressed in the future. Qualitatively, the MSR velocity solution reasonably reproduces the major flow features, as seen in the magnetogram movies, for all three examples discussed in §5. However, the MSR velocity field *does not* reproduce localized flows of emerging magnetic structures. There is no feedback from the MEF solution on this aspect, but the ILCT solution captures this feature since it relies on the LCT velocity which attributes a nonzero horizontal velocity to purely vertical flows. This discrepancy between the MSR and the ILCT results might be expected because the MSR method (and, apparently, the MEF method) relies only on the temporal variation of B_z and it cannot track down a particular feature, whereas the ILCT method exhibits a "memory" in identifying and tracking down individual magnetic features and interprets their

observed displacements by means of an assigned velocity. Moreover, the main approximation $u_{\perp_z} = 0$ of the MSR approach is expected to break down locally in areas of intense, rapid flux emergence or submergence.

Let us also underline that none of the existing inductive techniques can fully advance a given vector magnetogram in time to provide a short-term prediction for the evolution of the magnetic field vector based on the inferred inductive velocity. This would be useful for providing a continuous, or nearly continuous, boundary condition for data-driven 3D MHD models of the active-region corona. From single-height magnetic field measurements, however, only the vertical magnetic field can be advanced. Multi-height magnetic field measurements are absolutely necessary for advancing the horizontal magnetic field components.

Until recently, only the various tracking algorithms were available to assess the velocity field in solar active regions. There are now four different techniques, namely Kusano's et al. (2002) method, the ILCT method of Welsch et al. (2004), the MEF method of Longcope (2004), and the MSR method of this study, that use the ideal induction equation in an attempt to advance our understanding of the magnetized plasma flows. A comparative evaluation of all four techniques is underway and aims to realize the overall benefit furnished by the various methodologies. One envisions a consensus on an optimal velocity field calculation that will decisively improve our understanding of magnetized flows in solar active regions. A such scheme could incorporate elements from the existing techniques and should be open to future physically-founded ideas. These ideas might be incorporated into the solution of the induction equation by means of our general solving methodology.

REFERENCES

Abbett, W. P., AGU Fall Meeting 2003, Abstract #SM11A-03

Alissandrakis, C. E., 1981, A&A, 100, 197

Amari, T., Boulmezaoud, T. Z., & Mikić, Z., 1999, A&A, 350, 1051

Amari, T. Luciani, J. F., Aly, J. J., Mikić, Z., & Linker, J., 2003, ApJ, 595, 1231

Berger, M. A., 1999, Plasma Phys. Contr. Fusion, 41, 167

Berger, M. A., & Field, G. B., 1984, Journal Fluid Mech., 147, 133

Berger, Th. E., Löfdahl, M. G., Shine, R. S., & Title, A. M., 1998, ApJ, 495, 973

Bernasconi, P. N., Rust, D. M., Georgoulis, M. K., & LaBonte, B. J., 2002, SoPh, 209, 119

Boris, J. P., Landsberg, A. M., Oran, E. S., & Gardner, J. H., LCPFCT - Flux Corrected Transport Algorithm for Solving Generalized Continuity Equations, NRL/MR/6410-93-7192, p.23

Brown, D. S., Nightingale, R. W., Alexander, D., Schrijver, C. J., Metcalf, Th. R., Shine, R. A., Title, A. M., & Wolfson, C. J., 2003, SoPh, 216, 79

Chae, J., 2001, ApJ, 560, L95

Chae, J., Moon, Y.-J., & Pevtsov, A. A., 2004, ApJ, 602, L65

Démoulin, P., & Berger, M. A., 2003, SoPh, 215, 203

Diver, D. A., Brown, J. C., & Rust, D. M., 1996, SoPh, 168, 105

van Driel-Gesztelyi, L., Malherbe, J.-M., & Démoulin, P., 2000, A&A, 364, 845

Fan, Y., 2001, ApJ, 554, L111

Fisher, G. H., AGU Fall Meeting 2003, Abstract #SH51A-01

Gary, G. A., & Hagyard, M. J., 1990, SoPh, 126, 21

Gary, G. A., & Moore, R. L., 2004, ApJ, 611, 545

Georgoulis, M. K., & LaBonte, B. J., 2004, ApJ, 615, 1029

Georgoulis, M. K., LaBonte, B. J., & Metcalf, Th. R., 2004, ApJ, 602, 446

Georgoulis, M. K., Rust, D. M., Bernasconi, P. N., & Schmieder, B., 2002, ApJ, 575, 506

Gudiksen, B. V., & Nordlund, A., 2002, ApJ, 572, L113

Harvey, K., & Harvey, J., 1973, SoPh, 28, 61

Jackson, J. D., 1962, Classical Electrodynamics (New York: Wiley)

Kosovichev, A. G., 2002, AN 323, No. 3/4, 186

Kusano, K., Maeshiro, T., Yokoyama, T., & Sakurai, T., 2002, ApJ, 577, 501

Landolfi, M., & degl'Innocenti, E. L., 1982, SoPh, 78, 355

Lionello, R., Velli, M., Einaudi, G., & Mikić, Z., 1998, ApJ, 494, 840

Liu, Y., Jiang, Y., Ji, H., Zhang, H., & Wang, H., 2003, ApJ, 593, L137

Longcope, D. W., 2004, ApJ, 612, 1181

López Fuentes, M. C., Démoulin, P., Mandrini, C. H., Pevtsov, A. A., & van Driel-Gesztelyi, L., 2003, A&A, 397, 305

Magara, T., 2004, ApJ, 605, 480

Magara, T., & Longcope, D. W., 2003, ApJ, 586, 630

Metcalf, Th. R., Jiao, L., McClymont, A. N., Canfield, R. C., & Uitenbroek, H., 1995, ApJ, 439, 474

Meytlis, V. P., & Strauss, H. R., 1993, SoPh, 145, 111

Mickey, D. L., Canfield, R. C., LaBonte, B. J., Leka, K. D., Waterson, M. F., & Weber, H. M., 1996, SoPh, 168, 229

Moon, Y.-J., Chae, J., Wang, H., Choe, G. S., & Park, Y. D., 2002, ApJ, 580, 528

Nindos, A., & Zhang, H., 2002, ApJ, 573, L133

Nindos, A., & Zirin, H., 1998, SoPh, 182, 381

November, L. J., & Simon, G. W., 1988, 333, 427

Pariat, E., Aulanier, G., Schmieder, B., Georgoulis, M. K., Rust, D. M., & Bernasconi, P. N., 2004, ApJ, 614, 1099

Parker, E. N., 1966, ApJ, 145, 811

Pohjolainen, S., Maia, D., Pick, M., Vilmer, N., Khan, J. I., Otruba, W., Warmuth, A., Benz, A., Alissandrakis, C., & Thompson, B. J., 2001, ApJ, 566, 421

Press, W. H., Flannery, B. P., Teukolsky, S. A., & Vetterling, W. T., 1992, Numerical Recipes: The Art of Scientific Computing (New York: Cambridge Univ. Press), pp. 655 - 667

Priest, E. R., 1982, Solar Magnetohydrodynamics, (Dordrecht: Reidel Publishing Company), p. 102

Potts, H. E., Barrett, R. K., & Diver, D. A., 2004, A&A, 424, 253

Romano, P., Contarino, L., & Zuccarello, F., 2003, SoPh, 218, 137

Roudier, Th., Rieutord, M., Malherbe, J. M., & Vigneau, J., 1999, A&A, 349, 301

Roussev, I. I., Sokolov, I. V., Forbes, T. G., Gombosi, T. I., Lee, M. A., & Sakai, J. I., 2004, ApJ, 605, L73

Schmidt, H. U., 1964, in AAS-NASA Symposium on the Physics of Solar Flares, ed. W. N. Hess (NASA SP-50), 107

Sterling, A. C., & Moore, R. L., 2001, JGR, 106, A11, 25227

Strous, L. H., Scharmer, G., Tarbell, T. D., Title, A. M., & Zwaan, C., 1996, A&A, 306, 947

Thompson, B. J., Cliver, E. W., Nitta, N., Delanée, C., & Delaboudiniére, J.-P., 2000, GRL, 27, 1431

Wang, T., Yan, Y., Wang, J., Kurokawa, H., & Shibata, K., 2002, ApJ, 572, 580

Warmuth, A., Hanslmeier, A., Messerotti, A., Moretti, P.-F., & Otruba, W., 2000, SoPh, 194, 103

Welsch, B. T., Fisher, G. H., Abbett, W. P., & Regnier, S., 2004, ApJ, 610, 1148
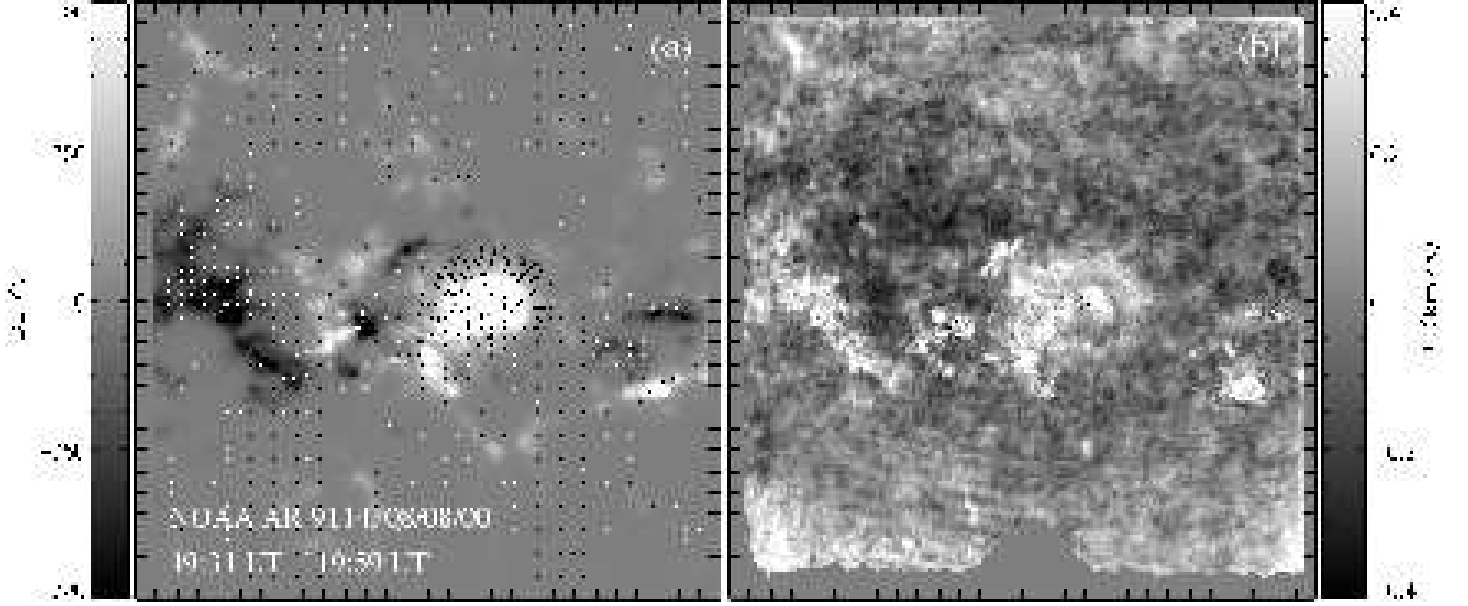
Fig. 1.— Average magnetic field and Doppler velocity in NOAA AR 9114 for a pair of vector magnetograms observed by the IVM on 2000 August 8 at 19:31 UT and at 19:59 UT, respectively. (a) Ambiguity-free average heliographic magnetic field vector on the image plane. A vector length equal to the tick mark separation corresponds to a horizontal magnetic field equal to 890 G. (b) Average Doppler velocity in the AR. Tick mark separation in both images is 10″.
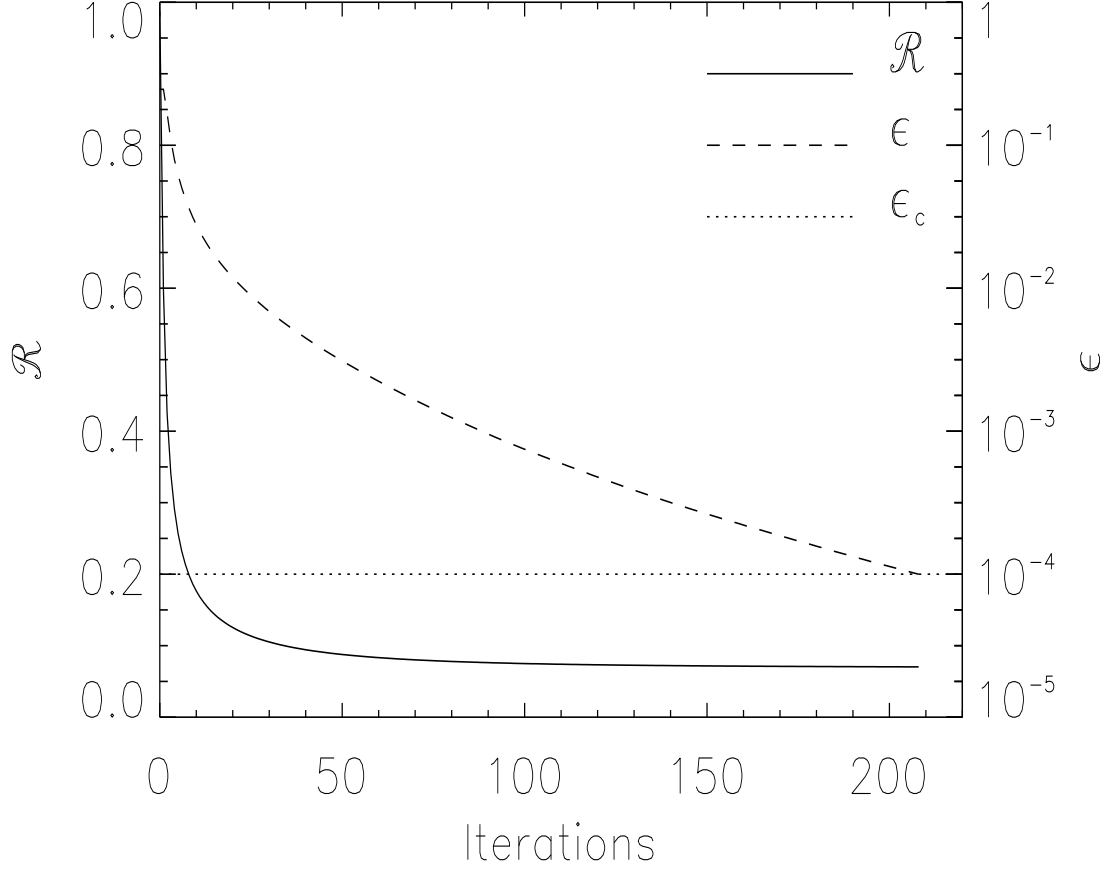
Fig. 2.— The convergence process in calculating the electrostatic field **G**. We show the minimization of the dimensionless ratio $\mathcal{R}$ (equation (19); solid line) and the fractional tolerance limit ε that controls the minimization process (equation (21); dashed line). The iterations stop when ε becomes smaller that a prescribed fractional tolerance limit ε_c, set to 10^{-4} (dotted line).
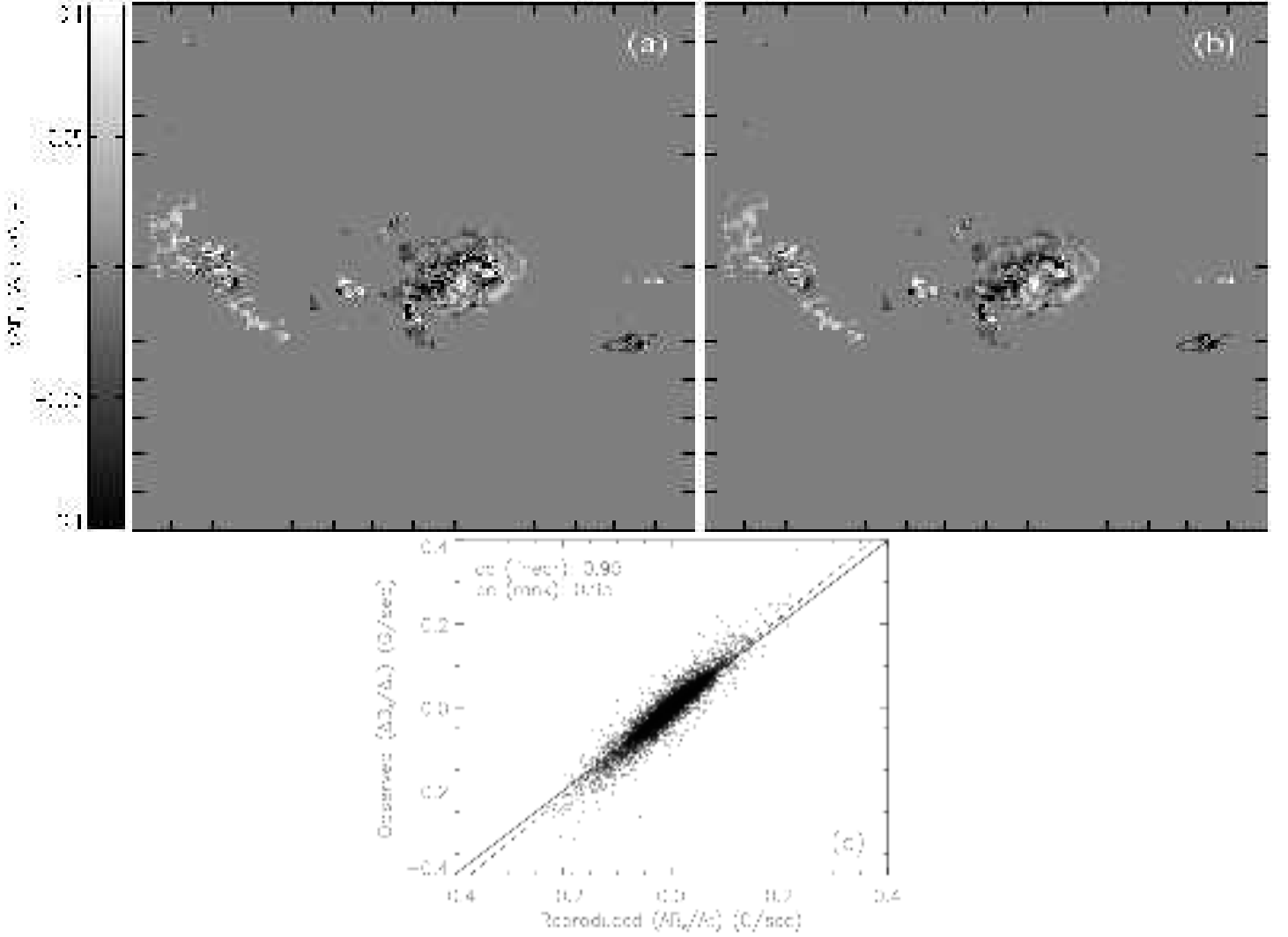
Fig. 3.— The temporal variation of the vertical magnetic field for the pair of magnetograms taken at 19:31 UT and at 19:59 UT in NOAA AR 9114: (a) Observed temporal variation. (b) Reproduced temporal variation, using the MSR velocity solution in the induction equation to solve for the vertical magnetic field (see text for details). Information is shown only for areas of strong magnetic fields. Tick mark separation in both images is 20″. (c) Comparison between the observed and the reproduced temporal variations. The dashed line corresponds to the best linear fit between the two quantities, while the analytical relation of equality is shown by the solid line. The linear and the Spearman rank correlation coefficients (cc) are also indicated.
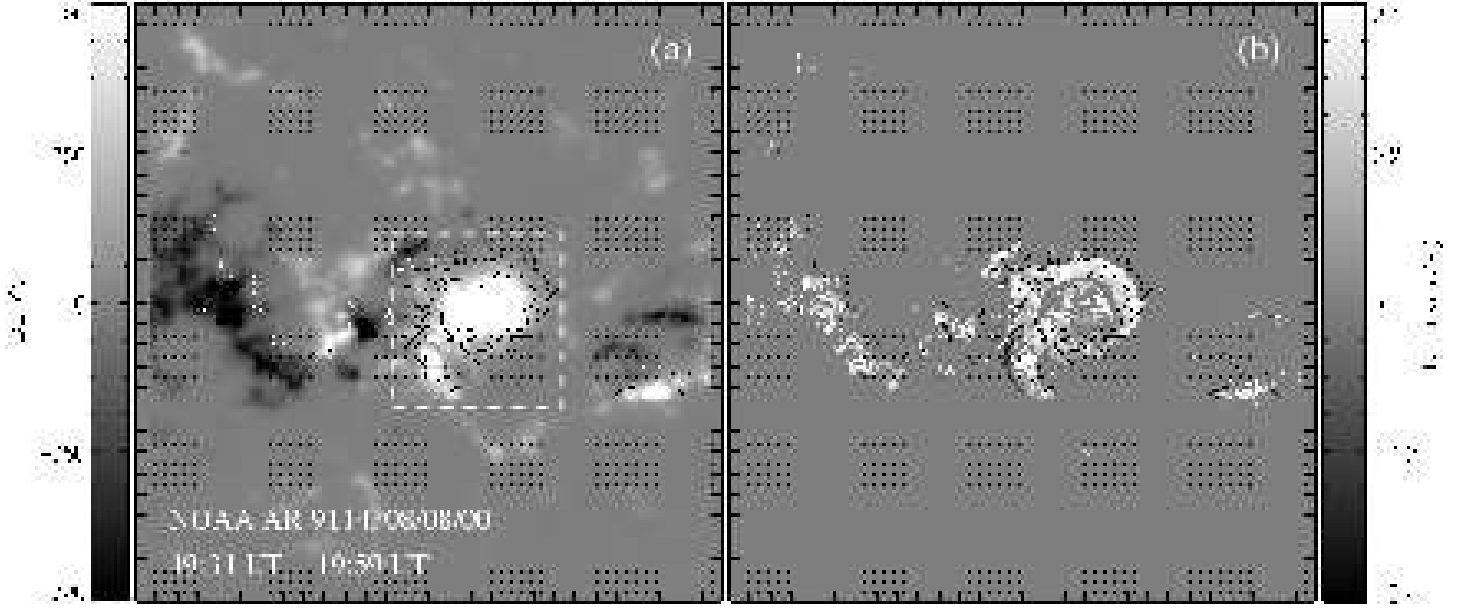
Fig. 4.— The MSR velocity field solution for the pair of magnetograms obtained at 19:31 UT and at 19:59 UT in NOAA AR 9114: (a) The horizontal velocity solution plotted on top of the average vertical magnetic field. The dashed rectangle encloses a rotating sunspot with distinctive outflows (see text for details). (b) The horizontal velocity solution plotted on top of the calculated vertical velocity. For both images, a vector length equal to the tick mark separation corresponds to a horizontal velocity field approximately equal to 1.5 $km\ s^{-1}$. Tick mark separation is 10″.
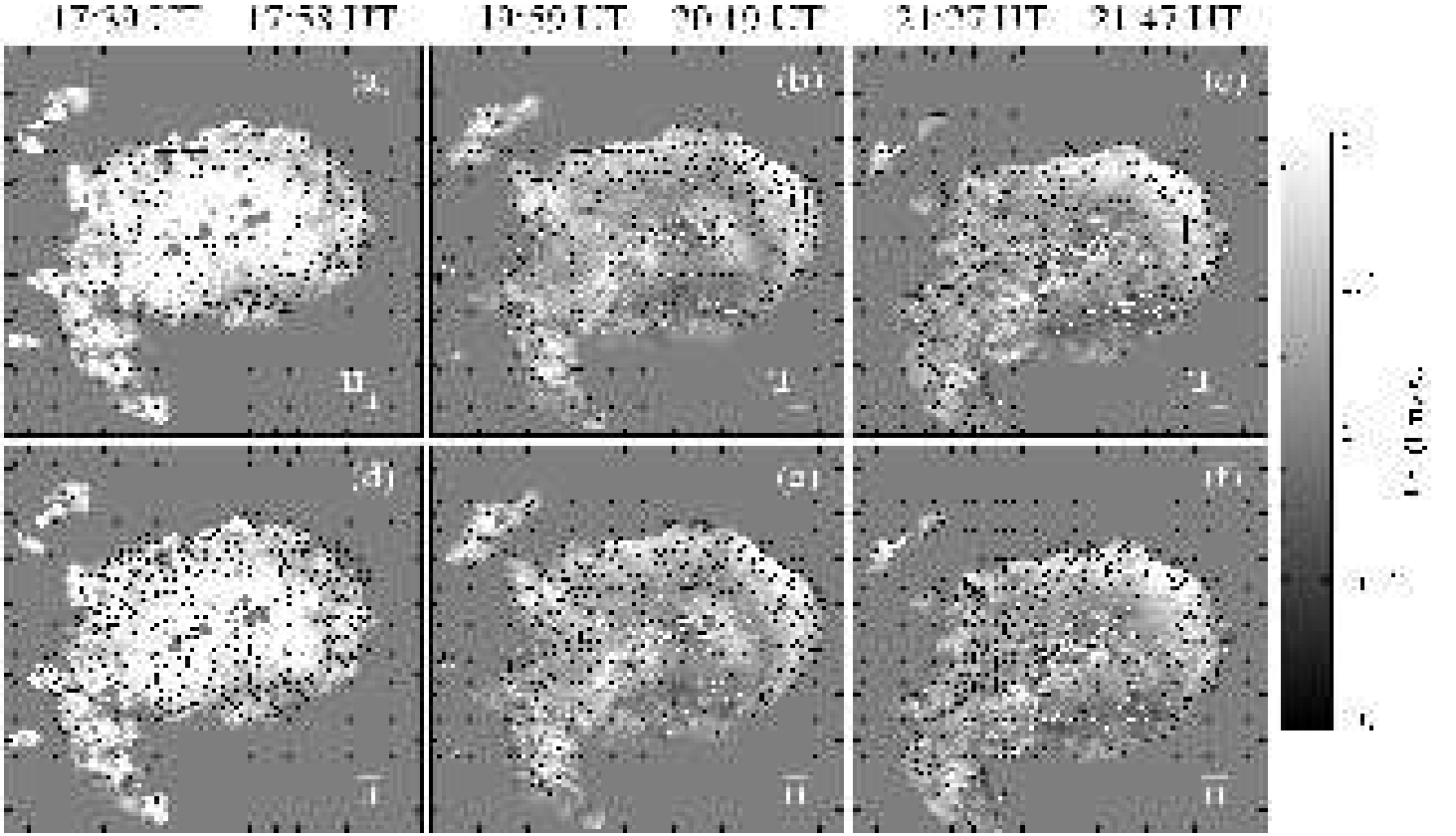
Fig. 5.— The MSR velocity field solution for a sub-region of NOAA AR 9114 indicated by the dashed rectangle in Figure 4a. Three different pairs of the AR vector magnetograms are used, obtained by the IVM on 2000 August 8. The times of each magnetogram pair are indicated at the top. The upper row of images (a, b, c) provides the horizontal cross-field velocity vector while the lower row of images (d, e, f) provides the total horizontal velocity vector, both plotted on top of the calculated vertical velocity. Each column of images (a,d; b,e; c,f) corresponds to the same pair of vector magnetograms. A vector length equal to the tick mark separation corresponds to a horizontal velocity field approximately equal to 1 $km\ s^{-1}$ in all images. Tick mark separation in all images is 5″.
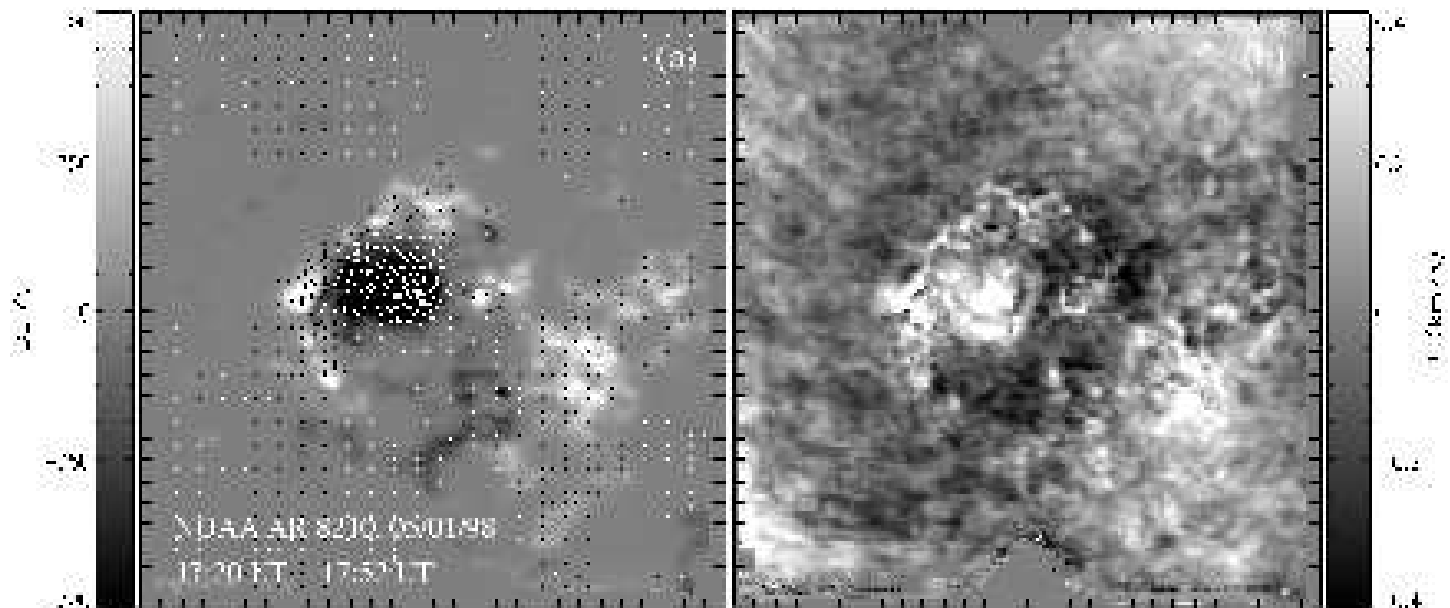
Fig. 6.— Average magnetic field and Doppler velocity in NOAA AR 8210 for a pair of vector magnetograms observed by the IVM on 1998 May 1 at 17:20 UT and at 17:52 UT, respectively. (a) Ambiguity-free average heliographic magnetic field vector on the image plane. A vector length equal to the tick mark separation corresponds to a horizontal magnetic field equal to 980 G. (b) Average Doppler velocity in the AR. Tick mark separation in both images is $10''$.
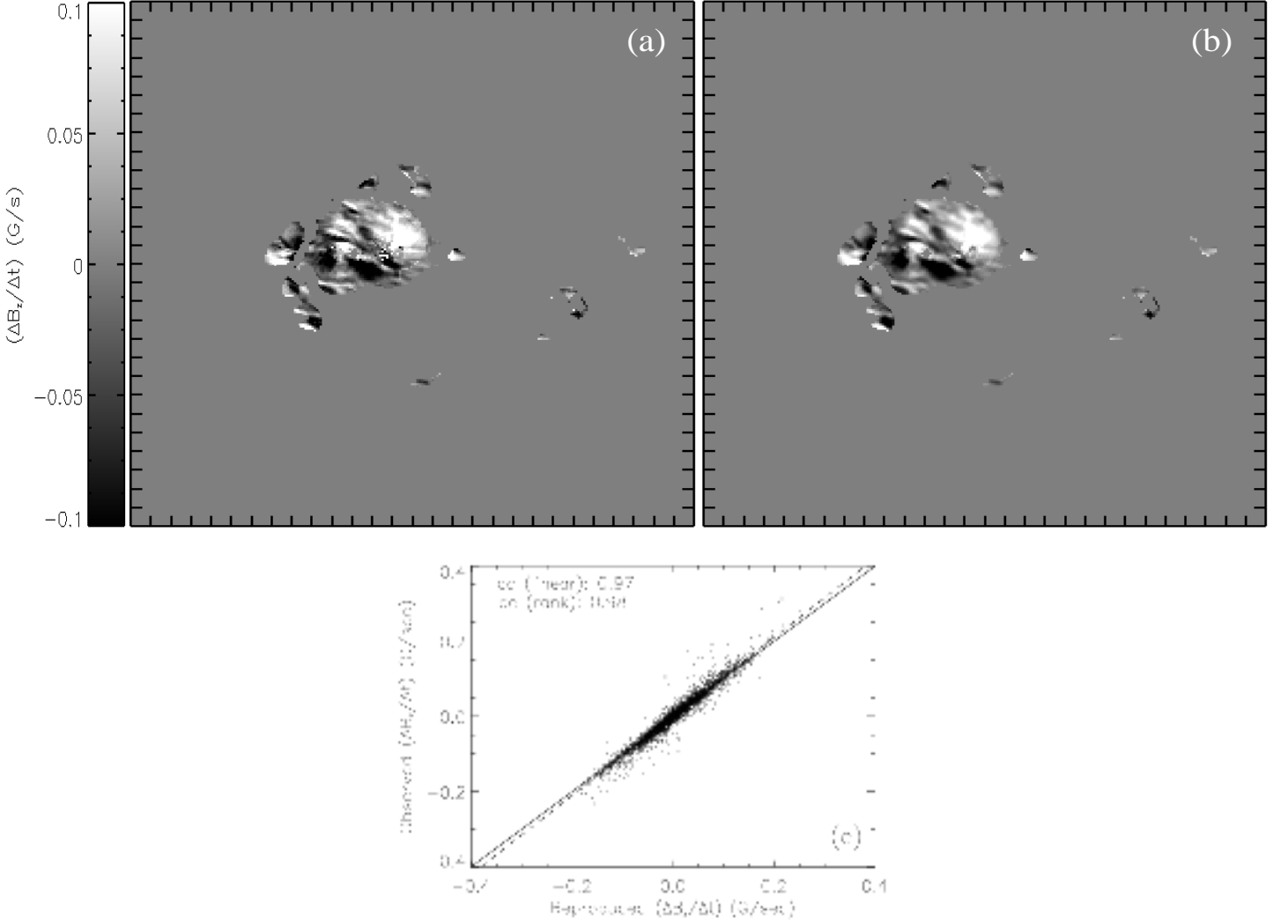
Fig. 7.— The temporal variation of the vertical magnetic field for the pair of magnetograms obtained at 17:20 UT and at 17:52 UT in NOAA AR 8210: (a) Observed temporal variation. (b) Reproduced temporal variation, using the MSR velocity solution in the induction equation to solve for the vertical magnetic field. Information is shown only for areas of strong magnetic fields. Tick mark separation in both images is $10''$. (c) Comparison between the observed and the reproduced temporal variations. The dashed line corresponds to the best linear fit between the two quantities, while the analytical relation of equality is shown by the solid line. The linear and the Spearman rank correlation coefficients (cc) are also indicated.
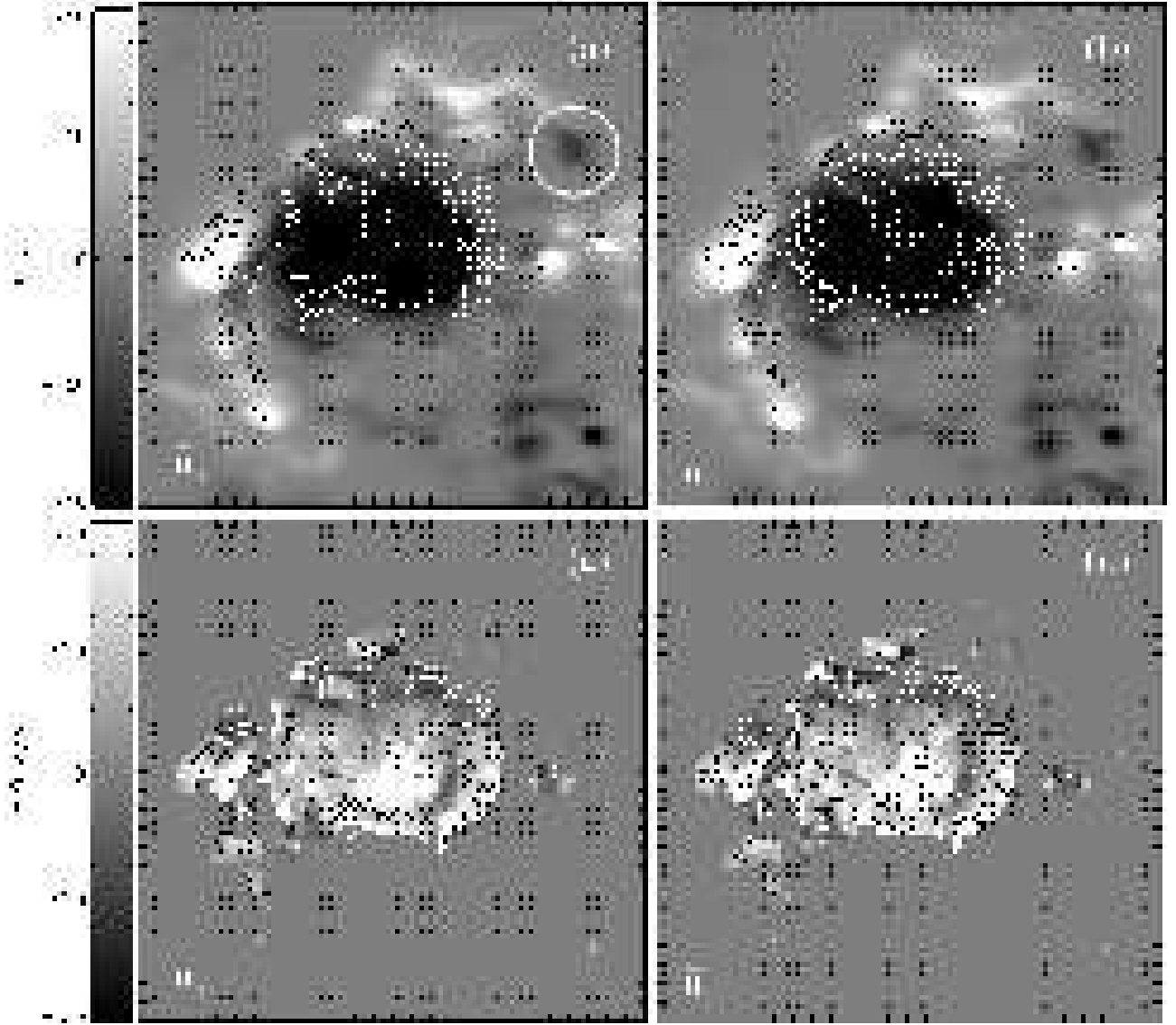
Fig. 8.— The MSR velocity field solution for the δ-sunspot in NOAA AR 8210, calculated for the pair of magnetograms obtained at 17:20 UT and at 17:52 UT. Only the calculated velocity for the strong-field regions is shown. The grayscale background in the upper row of images is the average vertical magnetic field, while for the lower row of images it is the vertical MSR velocity. The vector field in the left column of images corresponds to the cross-field MSR velocity $\mathbf{u}_\perp$ while in the right column of images it corresponds to the total MSR velocity $\mathbf{u}$. In all images, tick mark separation is $5''$. A vector length equal to the tick mark separation corresponds to a horizontal velocity of $\sim 1.15\ km\ s^{-1}$. The white oval in (a) indicates a small emerging flux sub-region discussed in the text.
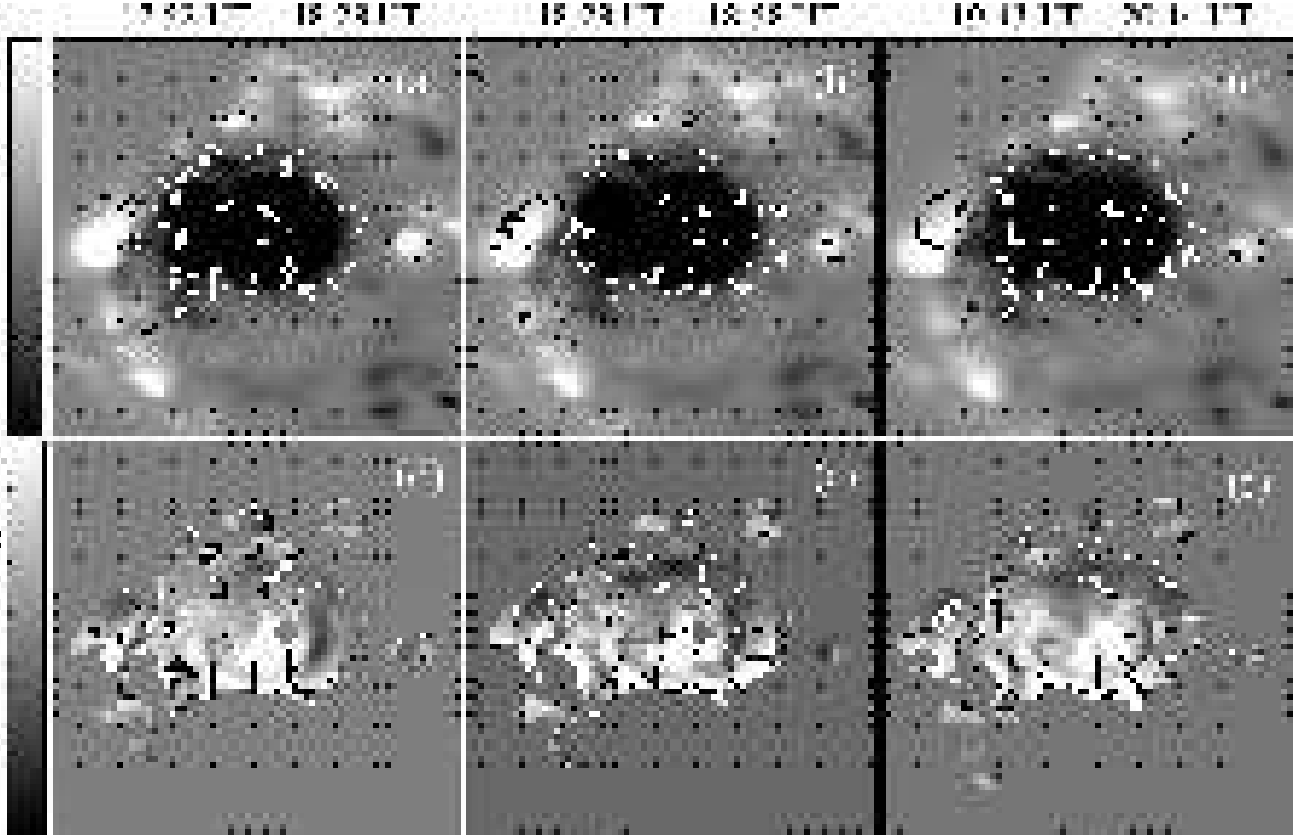
Fig. 9.— The MSR velocity field solution for the δ-sunspot in NOAA AR 8210 calculated for three different pairs of vector magnetograms obtained by the IVM on 1998 May 1. The vector field in each image corresponds to the total MSR velocity **u**. Each column of images corresponds to the same pair of magnetograms. The UT times of each pair are given at the top of each column of images. The grayscale background in the upper row of images corresponds to the average vertical magnetic field for each pair, while in the lower row of images it is the MSR vertical velocity. In all images, tick mark separation is $5''$. A vector length equal to the tick mark separation corresponds to a horizontal velocity of $\sim 1.3\ km\ s^{-1}$.
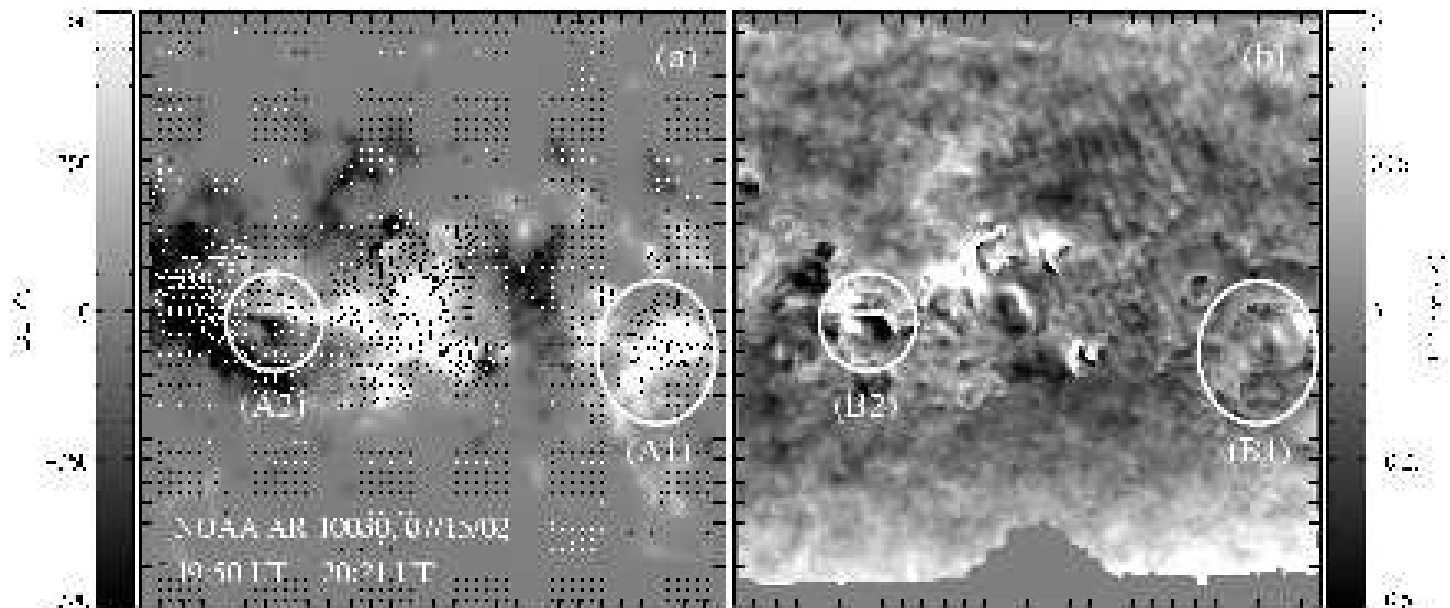
Fig. 10.— Average magnetic field and Doppler velocity in NOAA AR 10030 for a pair of vector magnetograms observed by the IVM on 2002 July 15 at 19:50 UT and at 20:21 UT, respectively. (a) Ambiguity-free average heliographic magnetic field vector on the image plane. A vector length equal to the tick mark separation corresponds to a horizontal magnetic field equal to 1250 G. (b) Average Doppler velocity in the AR. The white ovals correspond to two sub-regions of the AR discussed in the text. Tick mark separation in both images is $10''$.
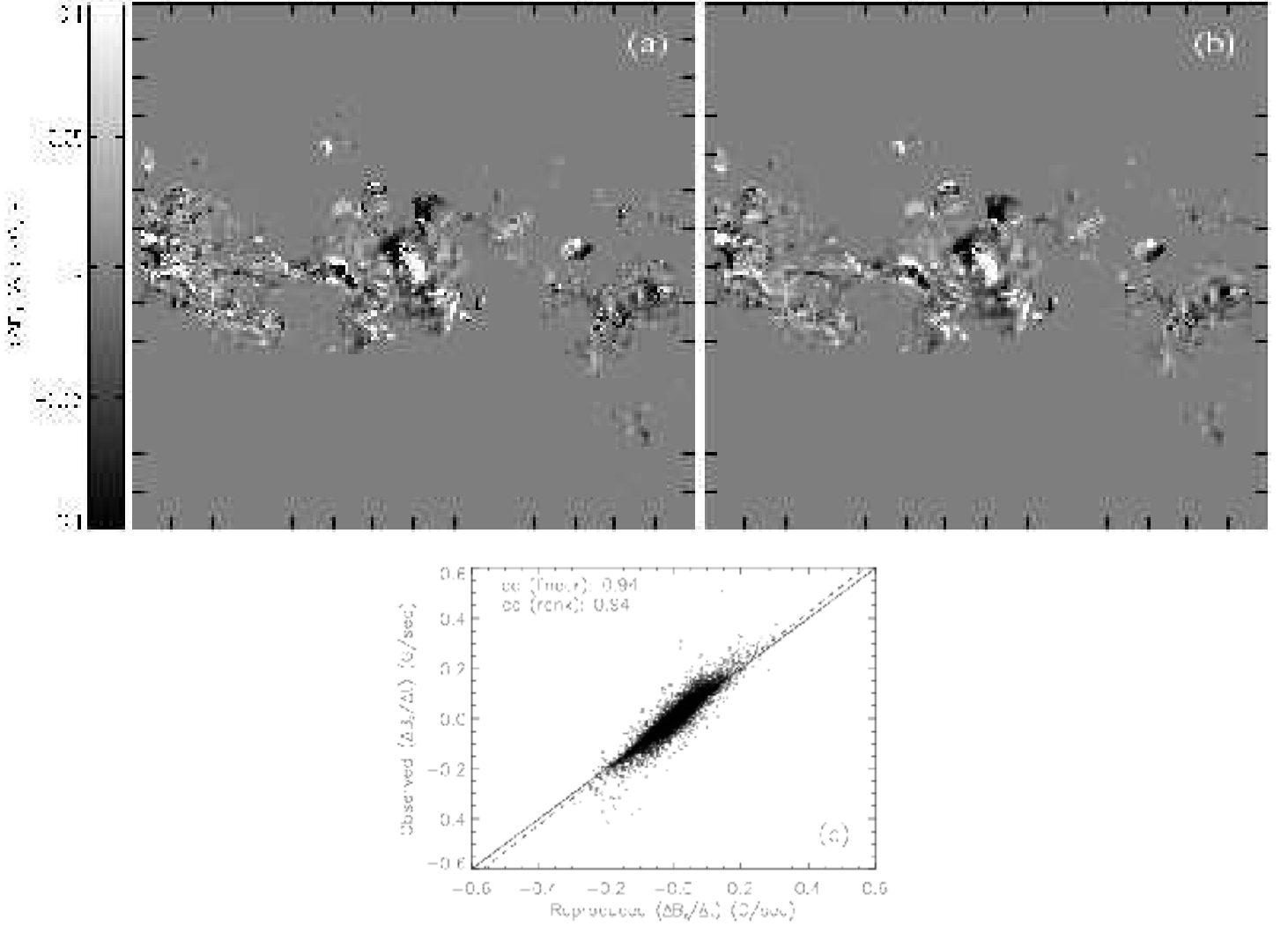
Fig. 11.— The temporal variation of the vertical magnetic field for the pair of magnetograms obtained at 19:50 UT and at 20:21 UT in NOAA AR 10030: (a) Observed temporal variation. (b) Reproduced temporal variation, using the MSR velocity solution in the induction equation to solve for the vertical magnetic field. Information is shown only for areas of strong magnetic fields. Tick mark separation in both images is $20''$. (c) Comparison between the observed and the reproduced temporal variations. The dashed line corresponds to the best linear fit between the two quantities, while the analytical relation of equality is shown by the solid line. The linear and the Spearman rank correlation coefficients (cc) are also indicated.
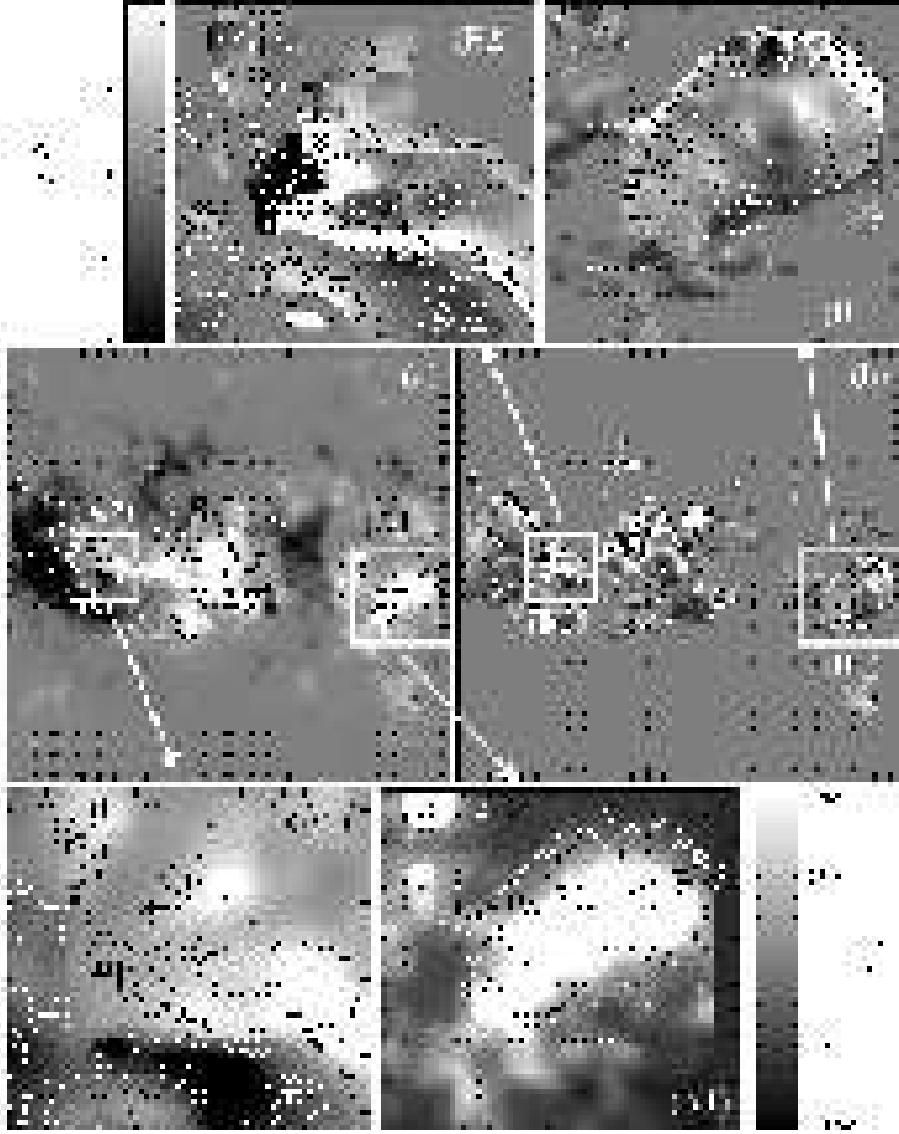
Fig. 12.— The MSR velocity field solution for the pair of vector magnetograms of NOAA AR 10030 obtained at 19:50 UT and at 20:21 UT. Only the velocity solution for the strong magnetic field regions is shown. (a) The horizontal velocity solution plotted on top of the average vertical magnetic field. (b) The horizontal velocity solution plotted on top of the calculated vertical velocity. Tick mark separation in (a) and (b) is 10″. A vector length equal to the tick mark separation in (a) and (b) corresponds to a horizontal velocity field of $\sim 1\ km\ s^{-1}$. Two details of the velocity solution have been magnified in (a) (details (A1) and (A2)) and (b) (details (B1) and (B2)). Tick mark separation in the details is 2″. A vector length equal to the tick mark separation in the details corresponds to a horizontal velocity field of $\sim 2\ km\ s^{-1}$.
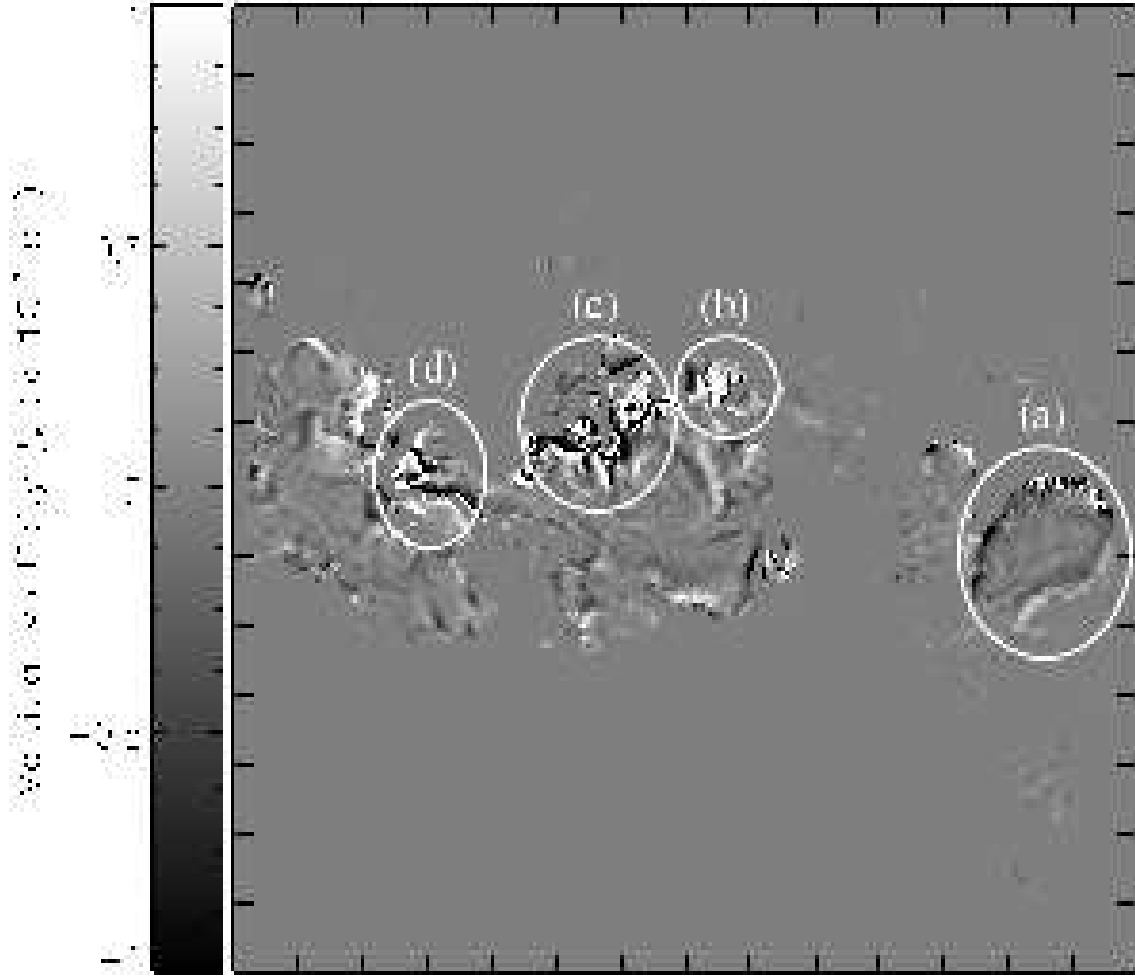
Fig. 13.— The vertical vorticity in NOAA AR 10030, calculated using the MSR velocity field solution for areas of strong magnetic field. Four extended areas of strong vorticity have been indicated by the ovals (a), (b), (c), and (d). Tick mark separation is 20″.